Enhanced inhibition of neuronal ferroptosis and regulation of microglial polarization with multifunctional traditional Chinese medicine active ingredients-based selenium nanoparticles for treating spinal cord injury

Luoqi Mai [a,b,1], Jinggong Liu [b,c,1], Huimei Wu [a,d], Hongshen Wang [c], Zhidong Lin [c], Siyuan Rao [c], Wenxi Sun [a], Aowei Tan [a], Yongpeng Lin [b,c,**], Bolai Chen [b,c,*]

[a] *Guangzhou University of Chinese Medicine, Guangzhou, 510120, China*

[b] *State Key Laboratory of Traditional Chinese Medicine Syndrome, The Second Clinical Medical College of Guangzhou University of Chinese Medicine, Guangzhou, 510120, China*

[c] *Orthopedics Department, The Second Clinical Medical College of Guangzhou University of Chinese Medicine, Guangzhou, 510120, China*

[d] *Dermatology Department, The Second Clinical Medical College of Guangzhou University of Chinese Medicine, Guangzhou, 510120, China*

A B S T R A C T

Spinal cord injury (SCI) is a devastating condition that results in the loss of sensory and motor functions. The complex pathogenesis of SCI contributes to the limited availability of effective therapies. Two major factors exacerbating secondary injury in SCI are neuronal ferroptosis and microglial inflammatory polarization. Tanshinone IIA (TSIIA) has demonstrated a significant anti-ferroptosis effect by inhibiting lipid peroxidation, while tetramethylpyrazine (TMP) exhibits remarkable anti-inflammatory properties by promoting the shift of microglial polarization from the M1 to the M2 phenotype. However, most drugs currently under development primarily target a single aspect of this multifaceted condition, which is insufficient for comprehensive treatment. Selenium nanoparticles have emerged as a promising therapeutic strategy due to their ability to encapsulate various agents, effectively targeting diverse pathophysiological mechanisms while offering favorable water solubility and low toxicity. In this study, we developed a novel nanocarrier functionalized with astragalus polysaccharide (APS) and loaded with TSIIA and TMP. Results from both *in vitro* and *in vivo* studies indicate that TSIIA/TMP/APS@Se NPs possess anti-ferroptosis properties and can regulate microglial polarization, potentially enhancing functional recovery following SCI. In summary, this study presents a promising alternative strategy for treating SCI, highlighting its significant potential for future clinical applications.

1. Introduction

Spinal cord injury (SCI) is a debilitating neurological condition that leads to lifelong disability and necessitates costly medical care, making it a significant global health concern due to the limited availability of effective treatment options [1,2]. Between 1990 and 2019, there was a notable increase in the global incidence, prevalence, and years lived with disability associated with SCI. In the United States alone, it is estimated that SCI incurs annual costs exceeding US$9.7 billion, placing an overwhelming burden on national finances and healthcare institutions [3]. One of the most pressing challenges is mitigating the damage caused by secondary injuries that follow the initial trauma [4–6]. Recent research has focused on neuronal ferroptosis and the exacerbation of the spinal cord microenvironment, both of which are interconnected and contribute to a vicious cycle that worsens secondary injury in SCI [7,8].

Ferroptosis is a newly identified form of programmed cell death characterized by iron-dependent and excessive intracellular lipid peroxidation. It has been shown to play a critical role in central nervous system (CNS) diseases, including SCI [9–11]. The disruption of spinal

---

cord tissue triggers a series of secondary injury events, such as local hemorrhage, ischemia, hypoxia, erythrocyte rupture, increased ferrous ion concentration, and excessive production of free radicals [12]. These changes can lead neurons to undergo ferroptosis when the system Xc-becomes overwhelmed. This overwhelm is attributed to the initiation of the Fenton reaction, the aggregation of polyunsaturated fatty acids, and the overproduction of lipid peroxides [11,13,14]. Numerous studies have demonstrated that inhibiting neuronal ferroptosis can promote neural regeneration and recovery following SCI [12,15,16].

Microglia, the resident macrophages of the CNS, play a crucial role in safeguarding and regulating the homeostasis of the microenvironment [17]. Polarization refers to the process by which microglia change their state to fulfill various functions in response to specific environmental conditions [18]. The M1 and M2 phenotypes represent two distinct polarized states of microglial cells, each exhibiting diverse functionalities that help maintain a dynamic and precise equilibrium within the body [19]. Over-activated M1 microglia initiate a strong inflammatory response, which can have detrimental effects on the immune microenvironment of the spinal cord. This response is characterized by the excessive release of pro-inflammatory factors, reactive oxygen species (ROS), colony-stimulating factors, and other related molecules [20]. In contrast, M2 microglia primarily facilitate neuroprotection through their involvement in phagocytosis and the release of anti-inflammatory mediators following SCI [21]. Increasing research indicates that inhibiting M1 polarization while promoting M2 polarization is a significant strategy for modulating the microenvironment in SCI to enhance recovery [22–26].

Microglial inflammatory polarization exacerbates neuronal ferroptosis by worsening the microenvironment [27]. Conversely, the accumulation of iron triggers abnormal activation of microglia [28]. Therefore, targeting both neuronal ferroptosis and the inflammatory polarization of microglia presents a promising therapeutic strategy.

Traditional Chinese medicine (TCM) represents a rich repository of therapeutic resources in China. Key ingredients extracted from herbs, such as Danshen (*Salvia miltiorrhiza Bunge*) and Chuanxiong (*Rhizoma Chuanxiong*), have been shown to perform various functions, including preventing neuronal death, alleviating neuroinflammation, and improving tissue microenvironments [29]. Tanshinone IIA (TSIIA), a primary component of Danshen, not only exhibits strong anti-ferroptosis capabilities to mitigate oxidative damage but also promotes functional recovery following SCI [30,31]. Similarly, tetramethylpyrazine (TMP), a major component of Chuanxiong, has been demonstrated to alleviate neuroinflammation by modulating microglial polarization [32,33]. Additionally, TMP inhibits the production of inflammatory factors such as TNF-α and IL-1β, facilitating spinal cord recovery [34]. However, these components primarily target single pathomechanism, which limit their overall therapeutic efficacy. Furthermore, TCM ingredients often have a short half-life and poor water solubility, significantly restricting their therapeutic potential. Therefore, it is essential to develop a novel delivery platform that is soluble, stable, and biocompatible, allowing for the simultaneous targeting of neuronal ferroptosis and microglial polarization with TCM components.

Selenium (Se), a trace element of exogenous origin, was first shown to be effective in improving SCI in experimental animals as early as 1985 [35]. Its mechanism of action is closely associated with its anti-inflammatory, anti-apoptotic, and ROS-scavenging properties [36]. Recent studies have surprisingly revealed that Se supplementation promotes recovery of neurological function after SCI by inhibiting neuronal ferroptosis [14,37,38]. Se treatment primarily reduces the concentration of ferric ions and the lipid peroxidation products malondialdehyde (MDA) and 4-hydroxynonenal (4-HNE) in SCI rats. Additionally, Se protects neurons and oligodendrocytes from ferroptosis while inhibiting the hyperproliferation of astrocytes by upregulating glutathione peroxidase 4 (GPX4) [37]. However, the narrow therapeutic window of Se is attributed to its suboptimal particle stability, which is characterized by uneven size and low biological activity [39]. Selenium

nanoparticles (Se NPs), which are nano-sized forms of elemental selenium, have garnered significant interest in biomedicine due to their excellent biocompatibility, favorable water solubility, and low toxicity [26,40,41]. These properties make them ideal carriers for developing novel drugs. In our previous study, we demonstrated that astragalus polysaccharide (APS), a primary component of Huangqi (*Radix Astragali*), is a suitable ingredient for functionalizing Se NPs to stabilize their structure [42]. Furthermore, inspired by the principles of TCM compatibility theory, we developed Se NPs by incorporating APS and TSIIA to enhance the therapeutic effects of TCM ingredients. This combination provides antioxidant properties, improves mitochondrial dysfunction, reduces cell apoptosis and S phase cell cycle arrest in PC12 cells [42]. Therefore, developing a stable, low-toxicity, long-acting nanoplatform that integrates TSIIA and TMP to effectively inhibit ferroptosis and inflammation in the treatment of SCI represents a promising strategy.

In this study, we successfully synthesized a novel multifunctional Se NPs (TSIIA/TMP/APS@Se NPs) functionalized with APS, TSIIA, and TMP. The TSIIA/TMP/APS@Se NPs demonstrated exceptional stability in both short-term and long-term aqueous solutions. Additionally, these nanoparticles effectively transport and release TCM ingredients within cells without exhibiting significant cytotoxicity. Moreover, the TSIIA/TMP/APS@Se NPs maintained the unique properties of each ingredient, including resistance to neuronal ferroptosis, regulation of microglial polarization, and alleviation of neuroinflammation in both *in vitro* and *in vivo* experiments. Furthermore, the TSIIA/TMP/APS@Se NPs reduced neuronal damage, promoted axonal regeneration, and attenuated glial scar formation in mice with SCI, thereby facilitating the rehabilitation of spinal cord function (Scheme 1.).

2. Materials and methods

2.1. Materials

APS, TSIIA, and TMP were purchased from Must Biotechnology Co., Ltd. Vitamin C, Na$_2$SeO$_3$, Coumarin-6, and Lysotracker were bought from Sigma-Aldrich.

Erastin was bought from MedChemExpress. BODIPY 581/591C11 was purchased from Dojindo Laboratories, Kumamoto, Japan. MDA Colorimetric Assay Kit, GSH Colorimetric Assay Kit, Total Iron Colorimetric Assay Kit, and Annexin-V Apoptosis Kit were purchased from Elabscience Biotechnology Co., Ltd. The cell count kit-8, DCFH-DA, Calcein/PI Assay Kit, JC-1 test kit were purchased from Shanghai Beyotime Biotechnology (China). The commercial Enzyme-Linked Immunosorbent Assay (ELISA) kits of TNF-α, IL-1β, IL-6, IL-10, APC anti-mouse CD206 (MMR) antibody (#141708), FITC anti-mouse CD16/32 antibody (#156614), and F4/80 (123119) antibody were purchased from BioLegend (San Diego, America). GPX4 (67763-1-Ig), FTH1 (11682-1-AP), iNOS (18985-1-AP), and Arg-1 (66129-1-lg) were brought from Proteintech Co., Ltd. xCT (ab307601) and MAP-2 antibody (#ab183830) were acquired from Abcam. NF 200 (GB15141-50), NeuN (GB15138-50), GFAP (GB12100-50), CD86 (GB300601-M-), and Iba-1 (GB15105) were bought from Servicebio Co., Ltd. 4-HNE(A24456) was purchased from Abclonal Co., Ltd. ABTS and DPPH commercially available kits were acquired from Solarbio Co., Ltd.

2.2. Synthesis of TSIIA/TMP/APS@Se NPs

First, 1 mL of the APS solution (20 mg/mL), 0.25 mL of TMP solution (1 mg/mL) and 0.25 mL of TSIIA solution (1 mg/mL) were mixed with 2 mL of the Na$_2$SeO$_3$ solution (20 mM) at the room temperature with stirring. Then, 2 mL of Vitamin C solution (40 mM) was introduced slowly into the mixture and further diluted with Milli-Q water up to a final volume of 10 mL. The mixture was then agitated for 12 h and subjected to dialysis against Milli-Q water for a duration of 24 h. The coumarin-6-labelled TSIIA/TMP/APS@Se NPs were synthesized by
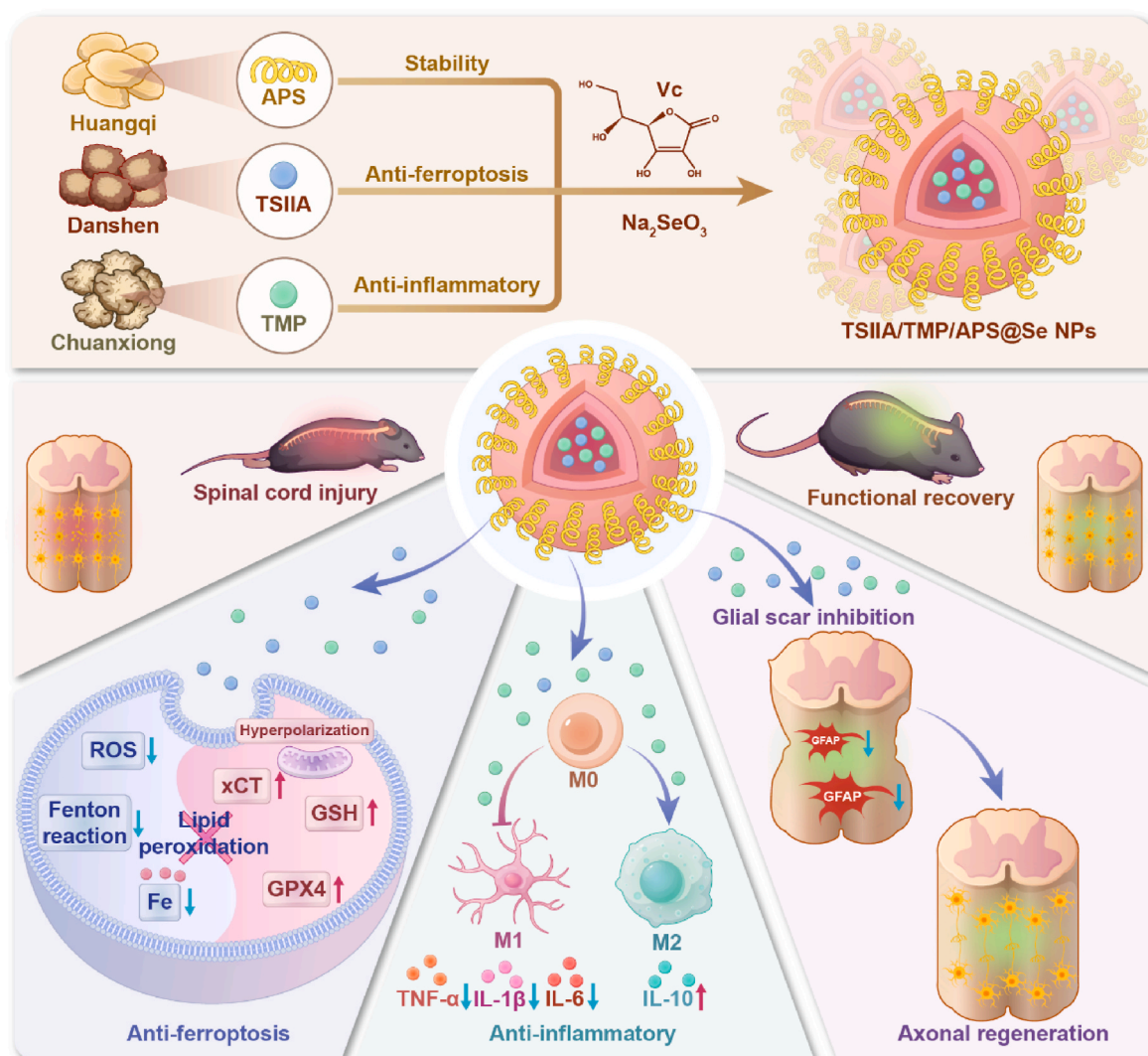
Scheme 1. Schematic illustration of the TSIIA/TMP/APS@Se NPs for the treatment of spinal cord injury.

adding the coumarin-6 solution into the mixture of Na_2SeO_3, APS, TMP, and TSIIA in the dark before adding vitamin C, as in our previous study [42].

2.3. Characterization of TSIIA/TMP/APS@Se NPs

The microstructure and elemental distribution of APS@Se NPs, TSIIA/APS@Se NPs, TMP/APS@Se NPs, and TSIIA/TMP/APS@Se NPs were obtained by transmission electron microscopy (TEM, JEM 2100 F) and HR-TEM (JEOL 2010). The hydration particle size distributions and zeta potentials were analyzed by using the Malvern Zetasizer-Nano instrument. XPS was conducted on Thermo Scientific KAlpha$^+$. The chemical structure was implemented by an FTIR-8300 series spectrometer (Shimadzu, Japan).

2.4. Free radical scavenging assay

The scavenging efficiency of TSIIA/TMP/APS@Se NPs for ABTS and DPPH was assessed by using commercially available kits in accordance with the respective protocols (Solarbio, BC4770 and BC4750).

2.5. Cellular uptake and intracellular trafficking of TSIIA/TMP/APS/@Se NPs

Flow cytometry: PC12 cells were incubated multiple times with coumarin-6-labelled TSIIA/TMP/APS@Se NPs (0.5 h, 1 h, 2 h, 4 h, and 6 h). The fluorescence intensity of coumarin-6-labelled TSIIA/TMP/APS@Se NPs in PC12 cells treated at different time points was detected by using Beckman Coulter CytoFLEX S (B75408).

Fluorescence images: PC12 cells were labelled with DAPI (1 μM), Lysotracker (80 nM) for 20 min and 2 h, respectively. Then, the cells were treated with 2.5 μM and 5 μM coumarin-6-labelled TSIIA/TMP/APS@Se NPs, and the route was visualized at different time points (0.5 h, 1 h, 2 h, 4 h, and 6 h) by using a fluorescence microscope (Nikon: ECLIPSE Ti2-E).

2.6. Cytotoxicity Evaluation.

The cytotoxicity of erastin, APS@Se NPs, TSIIA/APS@Se NPs, TMP/APS@Se NPs, and TSIIA/TMP/APS@Se NPs toward PC12 cells were measured by the CCK-8 assay. Then different concentrations of erastin (0 μM, 0.25 μM, 0.5 μM, 0.75 μM, 1 μM, 1.5 μM, 2 μM, 2.5 μM, and 3 μM), APS@Se NPs, TSIIA/APS@Se NPs, TMP/APS@Se NPs, and TSIIA/TMP/APS@Se NPs (0 μM, 2.5 μM, 5 μM, 10 μM, and 20 μM, respectively) were added to each well along with 100 μL of the sample solution and incubated for 24 h. After 24 h, 10 μL of CCK-8 solution was added to separate well and the plate was incubated for an additional 1 h. Finally,

the absorbance of each well was measured by using a microplate reader at 450 nm. The cell viability rate was calculated by using the following equation

$$Cell\ viability = \left(OD_{Sample} - OD_{Blank}\right) \ / \ \left(OD_{Control} - OD_{Blank}\right) \times 100\%.$$

All experiments were repeated thrice.

2.6. Assessment of the ferroptosis inhibition capability of TSIIA/TMP/APS@Se NPs in PC12 cells

Lipid peroxidation and the accumulation of ROS in PC12 cells were measured using BODIPY C11 and DCFH-DA. PC12 cells were seeded in six-well plates and cultured overnight. The following day, the cells were incubated with TSIIA/TMP/APS@Se NPs for 2 h. After this incubation, erastin (750 nM) was added, and the cells were co-cultured for an additional 24 h. At the end of the intervention, the medium was removed, and the cells were washed three times with phosphate-buffered saline (PBS). Subsequently, the cells were cultured with either BODIPY C11 (1 µM) or DCFH-DA (1 µM) solution for 30 min. Finally, lipid peroxidation and total ROS levels were visualized using flow cytometry (Beckman, USA) and a fluorescence microscope (Nikon ECLIPSE Ti2-E), recording fluorescence intensity at Ex/Em = 583/591 nm for BODIPY C11 and Ex/Em = 488/525 nm for DCFH-DA. Additionally, we assessed the distribution and accumulation of Fe^{2+} using the FerroOrange probes in PC12 cells. Labeling of Fe^{2+} was achieved by incubating the cells with FerroOrange solution for 30 min. Confocal laser scanning microscopy (CLSM) was then employed to visualize the distribution of Fe^{2+}. To quantitatively assess the levels of glutathione (GSH), total iron, and MDA in PC12 cells, commercial kits were used to measure these parameters following the aforementioned intervention. According to the manufacturer's instructions, the absorbance of GSH, total iron, and MDA in the PC12 cells was measured using a microplate reader and analyzed based on the provided equations. TEM images of the mitochondria in PC12 cells were obtained using a JEM 2100 F microscope. Additionally, the PC12 cells were incubated in a medium containing the JC-1 probes for 20 min to detect mitochondrial membrane potential (MMP) signals. The cells were then harvested for flow cytometry to analyze J-aggregates and J-monomers using PE and FITC, respectively. Simultaneously, fluorescence images of the MMP were captured using a fluorescence microscope.

2.7. Assessment of the anti-inflammation performance of TSIIA/TMP/APS@Se NPs in BV2 cells

To evaluate the anti-inflammatory effects of TSIIA/TMP/APS@Se NPs, the levels of TNF-α, IL-6, IL-1β, and IL-10 in the supernatants of BV2 cells were quantified using commercial ELISA kits according to the manufacturer's instructions. Additionally, to assess microglial polarization, BV2 cells were treated with TSIIA/TMP/APS@Se NPs 2 h after being seeded in six-well plates. The BV2 cells were then cultured with TSIIA/TMP/APS@Se NPs (5 µM) and 1 µg/mL LPS for 10 h. Afterward, the cells were harvested, and the ratios of M1 (CD16/32 and F4/80 double positive) to M2 (CD206 and F4/80 double positive) phenotypes were determined using flow cytometry.

2.8. Co-culture of PC12 cells and BV2 cells

Pre-saturate the polycarbonate membrane of the transwell chamber with DMEM before incubating the cells. A total of 2×10^4 BV2 cells were seeded in the upper chamber. After 12 h, 2×10^4 PC12 cells were seeded in the lower chamber with a complete medium. The BV2 cells were then preincubated with TSIIA/TMP/APS@Se NPs for 2 h before being activated with LPS (1 µg/mL) for 10 h. Once activated, the BV2 cells were transferred to the lower compartment for an additional 24 h to allow the PC12 cells to adhere. Finally, the PC12 cells were collected and used for

Live/Dead experiments and Annexin V-FITC/PI flow cytometry, following the protocols of the Calcein/PI Cell Viability Kit and the Annexin V-FITC/PI Apoptosis Detection Kit, respectively.

2.9. Western blot

Both cells and spinal cord tissue proteins were extracted using RIPA lysis buffer containing protease inhibitors (in a 100:1 ratio). After ultrasonic treatment to lyse the cells, the protein concentration was measured using a BCA kit. Protein electrophoresis was conducted on 8 %, 10 %, and 12 % SDS-PAGE gels, and the proteins were then transferred to a PVDF membrane (Merck Millipore, USA). The membranes were blocked with 5 % skim milk for 1 h following the transfer. Subsequently, the membranes were incubated overnight at 4 °C with primary antibodies (GPX4, xCT, FTH1, iNOS, Arg-1). The next day, after washing, the membranes were incubated with secondary antibodies. Protein bands were visualized using an ECL kit (Millipore, USA) and imaged with a Bio-Rad ChemiDoc imaging system. The gray values of all bands were quantified using ImageJ. The quantitative results from all western blot analyses were obtained from three independent experiments.

2.10. Animal model of SCI and tissue preparation

Two-month-old female C57BL/6 mice, weighing between 20 and 25 g, were purchased from the Guangdong Medical Laboratory Animal Center (Guangdong, China). All mice were treated in accordance with the approved experimental protocols established by the Institutional Animal Care and Use Committee at Daoke Medical & Pharmaceutical Company (Guangzhou, China) (Approval number: IACUC-DK-2023-07-05-01).

The SCI model was established following the methodology outlined in a previous study [43]. Briefly, the mouse was anesthetized with 1 % pentobarbital sodium, and a laminectomy was performed at the T10 segment under aseptic conditions. The SCI was induced using parameters of 0.6 mm impact depth, 0.5 m/s impact speed, and an 80 ms retention duration, utilizing the PinPoint™ precision impactor device (PCI3000-2, Hatteras Instrument, USA). The skin, muscle, and fascia were then closed in layers, and the outer skin was sterilized using iodophors. Mice in the sham group underwent laminectomy surgery without any additional impact injury to the spinal cord. Each mouse received intramuscular injections of penicillin for 3 days and underwent manual bladder massage twice daily until bladder function was restored. The mice were divided into four groups: the sham group, the SCI group, the APS@Se NPs group, and the TSIIA/TMP/APS@Se NPs group. Mice in the APS@Se NPs group and the TSIIA/TMP/APS@Se NPs group were treated with APS@Se NPs solution (dissolved in saline, 1 mg/kg) and TSIIA/TMP/APS@Se NPs solution (1 mg/kg), respectively, via tail vein injection three times a week. Mice in the sham group and SCI group received saline treatment via tail vein injection three times a week as well. Seven days after the injury, some of the mice were sacrificed to investigate the anti-ferroptosis effects of TSIIA/TMP/APS@Se NPs. Cardiac perfusion with paraformaldehyde was performed to fix the tissues. The levels of GPX4 and NeuN were evaluated using immunofluorescence, while lipid peroxidation levels were assessed through 4-HNE immunofluorescence. The remaining tissues were homogenized in RIPA lysis buffer for western blot analysis. Fourteen days after the injury, the spinal cord tissue was homogenized in PBS. After centrifugation of the tissue, the supernatant was used to detect inflammatory cytokines, including TNF-α, IL-6, IL-1β, and IL-10, using a commercial ELISA kit. The remaining tissues were lysed with RIPA buffer for western blot analysis. At this stage, the levels of Iba-1, CD86, and CD206 immunofluorescence in the spinal cord were measured. Following the completion of the treatment, hematoxylin and eosin (H&E) staining, Nissl staining, and immunofluorescence for GFAP, NeuN, NF-200, and MAP-2 in the spinal cord were conducted.

2.11. Behavioral analysis

Behavioral assessments were conducted using the basso mouse scale (BMS) score, inclined plane test, footprint analysis, and hindlimbs movement analysis. The BMS score is a standardized measure used to evaluate hindlimbs joint movements, gait coordination, and weight support in research studies. It ranges from 0 to 9 points, with 0 indicating paralysis and 9 indicating normal gait. The performance of the mice was assessed at various time points (1 day, 3 days, 1 week, 2 weeks, 3 weeks, and 4 weeks post-injury). The inclined plane test was performed to determine the maximum angle at which the mice could maintain a standing position for 5 s. For the footprint analysis, the hindlimbs of the mice were soaked in black dye and the fore limbs soaked in red before they walked through a narrow pathway to capture their footprints. We then quantified the distance between the anterior and posterior footprints of a single foot, referred to as stride length.

Additionally, we measured the vertical distance between the left and right feet within a single gait cycle. The footprints were scanned, and the data were analyzed to create digitized images. Hindlimbs movement analysis was conducted through video recordings as the mice traversed a runway. The sequence of movements-stamp, propel, lift, swing, and stamp-was meticulously documented.

2.12. Statistical analysis

The results are presented as the mean $\pm$ standard deviation, based on a minimum of three independent measurements. Further analysis was performed using one-way analysis of variance (ANOVA) with Bonferroni multiple comparison tests in SPSS software (version 13.0; Social Inc., IL, Chicago, USA). Statistical visualization was conducted using GraphPad Prism 9.0. $p < 0.05$ was considered to indicate statistically significant differences.
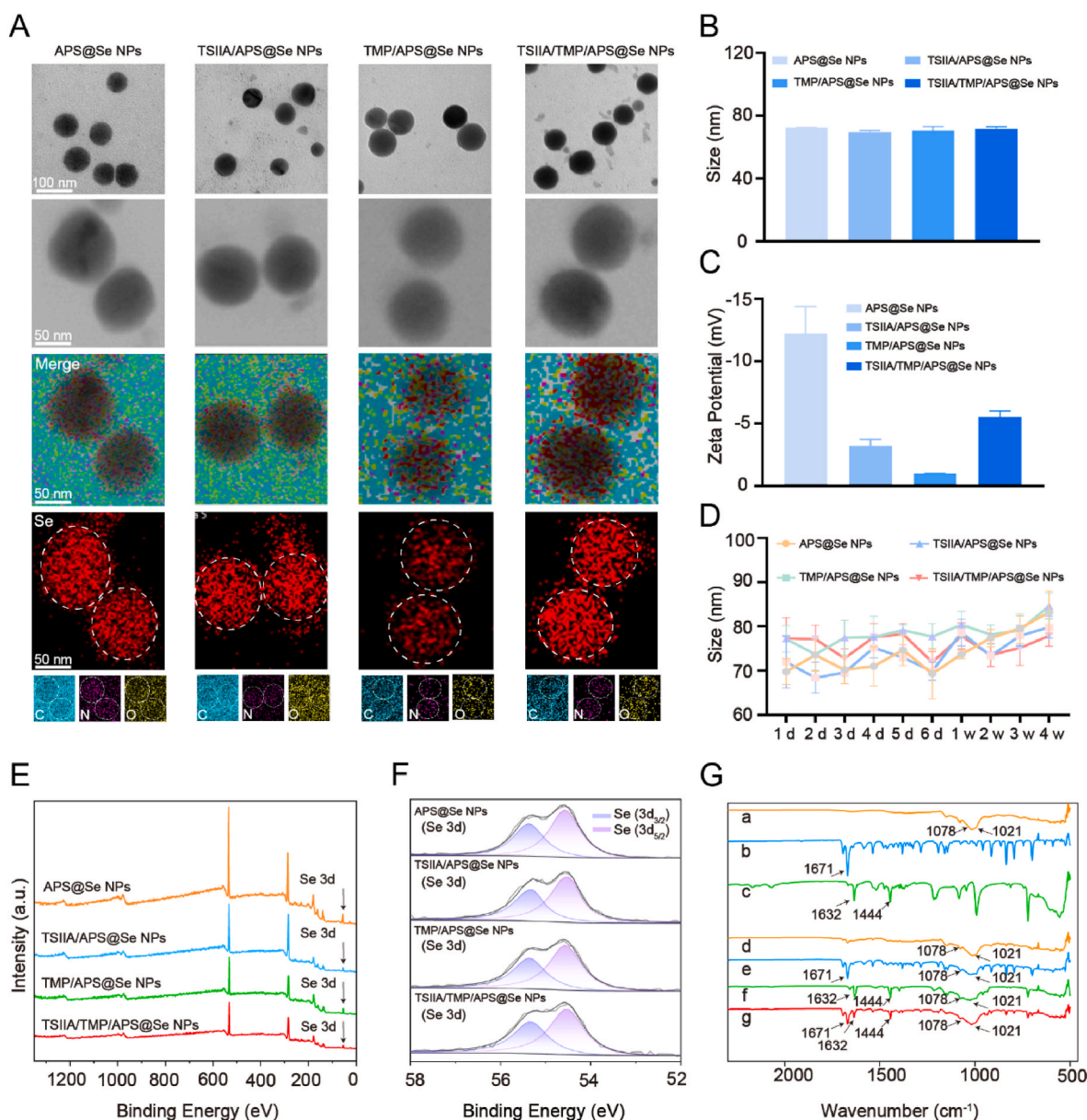

Fig. 1. Characterization of TSIIA/TMP/APS@Se NPs. (A) TEM images and element mapping of APS@Se NPs, TSIIA/APS@Se NPs, TMP/APS@Se NPs, and TSIIA/TMP/APS@Se NPs. (B) Particle size and (C) Zeta potential of APS@Se NPs, TSIIA/APS@Se NPs, TMP/APS@Se NPs, and TSIIA/TMP/APS@Se NPs. (D) The particle size distribution of APS@Se NPs, TSIIA/APS@Se NPs, TMP/APS@Se NPs, and TSIIA/TMP/APS@Se NPs with time progression. (E) XPS and (F) Se 3d spectra of APS@Se NPs, TSIIA/APS@Se NPs, TMP/APS@Se NPs, and TSIIA/TMP/APS@Se NPs. (G) FT-IR spectra of (a) APS, (b) TSIIA, (c) TMP, (d) APS@Se NPs, (e) TSIIA/APS@Se NPs, (f) TMP/APS@Se NPs, (g) TSIIA/TMP/APS@Se NPs.

3. Results and discussion

3.1. Characterization and free radical scavenging performance of TSIIA/TMP/APS@Se NPs

The APS@Se NPs, TSIIA/APS@Se NPs, TMP/APS@Se NPs, and TSIIA/TMP/APS@Se NPs were successfully synthesized through the reduction of sodium selenite using vitamin C, followed by encapsulation with APS to enhance their stability and biocompatibility. As shown in Fig. 1A, the four types of Se NPs exhibited a spherical morphology with an average size of approximately 70 nm, as visualized by TEM analysis. The hydrodynamic particle size distribution was consistent with the TEM results (Fig. 1B). After functionalization with APS, the TSIIA/APS@Se NPs, TMP/APS@Se NPs, and TSIIA/TMP/APS@Se NPs all maintained a negative zeta potential. Among these, the absolute value of the zeta potential for TSIIA/TMP/APS@Se NPs (5.52 ± 0.47 mV) was higher than that of the other two Se NPs (TSIIA/APS@Se NPs and TMP/APS@Se NPs), indicating that the TSIIA/TMP/APS@Se NPs exhibited robust and stable interactions, which contributed to the overall stability of the dispersion system (Fig. 1C). Subsequently, the long-term stability of Se NPs in aqueous solution was evaluated by measuring variations in their particle size. Notably, the particle size of TSIIA/TMP/APS@Se NPs fluctuated between 77 ± 4.7 nm after 1 day and remained stable at 78 ± 2.3 nm after 4 weeks. In contrast, the particle size of the other groups increased by 7–14 nm to varying extents (Fig. 1D). These results indicated that the four types of TCM-based Se NPs developed in this study exhibited excellent short-term and long-term stability in aqueous solution, particularly the TSIIA/TMP/APS@Se NPs, which is consistent with our previous.

findings [42]. X-ray photoelectron spectroscopy (XPS) and Fourier transformed-infrared spectroscopy (FT-IR) were performed to further verify the chemical structure of the four types of nanoparticles. In our previous study, we compared the valence states of selenium between APS@Se NPs and naked Se NPs to confirm the interaction between APS and Se, which contributes to the enhanced stability of Se NPs [42]. Currently, as shown in Fig. 1E and F, the XPS spectrum revealed the presence of Se 3d, indicating that all nanoparticles co-loaded with different ingredients decorated with APS consistently exhibit the valence states of Se $3d_{3/2}$ and Se $3d_{5/2}$, similar to APS@Se NPs. The FT-IR analysis showed that TSIIA/TMP/APS@Se NPs exhibited asymmetric vibrations of the C-O-C glycosidic bond, with peaks at 1021 cm^{-1} and 1078 cm^{-1}, as illustrated in Fig. 1G. These peaks correspond to the characteristic features of APS [44]. Additionally, the FT-IR spectrum of TSIIA/TMP/APS@Se NPs displayed the characteristic peak for the C=O stretching vibration at 1671 cm^{-1}, which is associated with TSIIA [45]. Furthermore, the spectrum revealed the main characteristic peaks of TMP at 1632 cm^{-1} and 1444 cm^{-1}, corresponding to the stretching vibrations of C=N, C=C, and C-N from TMP [46,47]. Together, these results confirmed the successful construction of TSIIA/TMP/APS@Se NPs. Subsequently, the free radical scavenging efficiency of the fabricated nanoparticles was assessed using the 2,2′-Azinobis-(3-ethylbenzthiazoline-6-sulfonate) (ABTS) and 1,1-diphenyl-2-picryl-hydrazyl (DPPH) assays. The antioxidant capacity of TSIIA/TMP/APS@Se NPs increased with higher concentrations, as evidenced by the reduction in color intensity of ABTS$^{•+}$ and DPPH (Figs. S1C–S1E). The TSIIA/TMP/APS@Se NPs demonstrated superior ABTS$^{•+}$ scavenging ability compared to the other three nanoparticles, as shown in Fig. S1A. Furthermore, Fig. S1B indicated that the DPPH scavenging efficacy of TSIIA/TMP/APS@Se NPs was 29.3 %, which was higher than that of the other nanoparticles: APS@Se NPs (20.1 %), TSIIA/APS@Se NPs (24.3 %), and TMP/APS@Se NPs (21.2 %). These findings suggested that TSIIA/TMP/APS@Se NPs possess outstanding free radical scavenging efficiency, followed by TSIIA/APS@Se NPs, TMP/APS@Se NPs, and APS@ Se NPs.

3.2. Cellular uptake, location, and cytotoxicity of TSIIA/TMP/APS@Se NPs

Effective internalization, release, and prolonged intracellular retention of nanoparticles are essential for their function as delivery carriers [48]. The fluorescent dye coumarin-6 is widely used for labeling cells and tissues, monitoring drug delivery systems, and imaging with fluorescence microscopy due to its unique fluorescent properties [49]. To visualize and quantify the uptake of nanoparticles by PC12 cells at various time points, we incorporated coumarin-6 into the TSIIA/TMP/APS@Se NPs (TSIIA/TMP/APS/Cur6@Se NPs) and tracked their progress using flow cytometry and fluorescence microscopy (Fig. 2A-C). Flow cytometry results showed that the absorption capacity of TSIIA/TMP/APS/Cur6@Se NPs by PC12 cells increased in a concentration- and time-dependent manner. Within 0.5 h post-intervention, 69.2 % of the TSIIA/TMP/APS/Cur6@Se NPs (5 μM) were internalized by PC12 cells, exhibiting an absorption level over 44 % higher than that observed with a concentration of 2.5 μM. Furthermore, more than 97 % of TSIIA/TMP/APS/Cur6@Se NPs (5 μM) were taken up by PC12 cells within 1–6 h, demonstrating prolonged retention in the cells (Fig. 2A). Next, we aim to investigate the intracellular localization of TSIIA/TMP/APS@Se NPs following endocytosis. Lysosomes play a crucial role in the intracellular processing of nanoparticles. After endocytosis, the nanoparticles accumulate in the lysosome and escaped from it and translocate into the cytoplasm to exert their function [50, 51]. We utilized Lysotracker, a specific fluorescence probe for lysosome, to visualize the processing of TSIIA/TMP/APS@Se NPs. The TSIIA/TMP/APS@Se NPs (5 μM) were labelled with coumarin-6 (green) as a fluorescent probe, while Lysotracker (red) and DAPI (blue) served as markers for lysosomes and nuclei, respectively. The fluorescence imaging results demonstrated a concentration- and time-dependent increase in the fluorescence levels of TSIIA/TMP/APS/Cur6@Se NPs, which is consistent with the findings from flow cytometry. The green fluorescence intensity peaked at 6 h. Additionally, we observed clear co-localization of TSIIA/TMP/APS/Cur6@Se NPs and Lysotracker within the time range of 0.5–6 h as time elapsed, indicating that Se NPs mainly located in lysosomes (Fig. 2B and C). These results clearly demonstrated that the nanoparticles are internalized and processed within the lysosomal pathway. Se NPs have garnered significant interest due to their lower toxicity compared to both inorganic.

and organic selenium [40,52]. Therefore, our initial assessment focused on determining the safe dosage range for different types of Se NPs. The results revealed that APS@Se NPs, TSIIA/APS@Se NPs, TMP/APS@Se NPs, and TSIIA/TMP/APS@Se NPs exhibited no cytotoxic effects on PC12 cells within the concentration range of 0–20 μM (Fig. 2D-G). Taken together, these findings suggested that TSIIA/TMP/APS@Se NPs (0–20 μM) do not cause cytotoxicity and exert their function through lysosomal degradation in cells.

3.3. TSIIA/TMP/APS@Se NPs protect PC12 cells from ferropotosis in vitro

PC12 cells were selected due to their widespread use as an *in vitro* model for investigating neuronal injury and neurodegenerative diseases [53]. Erastin, a classic small molecule inhibitor of the cystine-glutamate antiporter system, was employed to establish an *in vitro* model of ferroptosis in SCI [54]. In this study, PC12 cells served as a neuronal cell model, and erastin was used to establish the ferroptosis model. Subsequently, we evaluated ferroptosis in PC12 cells by assessing cell viability, the content of ferric and total iron ions, ROS levels, lipid peroxidation levels, and the expression of proteins related to the system Xc-. Initially, PC12 cells were exposed to a range of erastin concentrations for 24 h to determine the optimal concentration for inducing the ferroptosis model. The results of the CCK-8 assay showed a gradual decrease in PC12 cell viability with increasing concentrations of erastin, indicating the successful establishment of the ferroptosis model
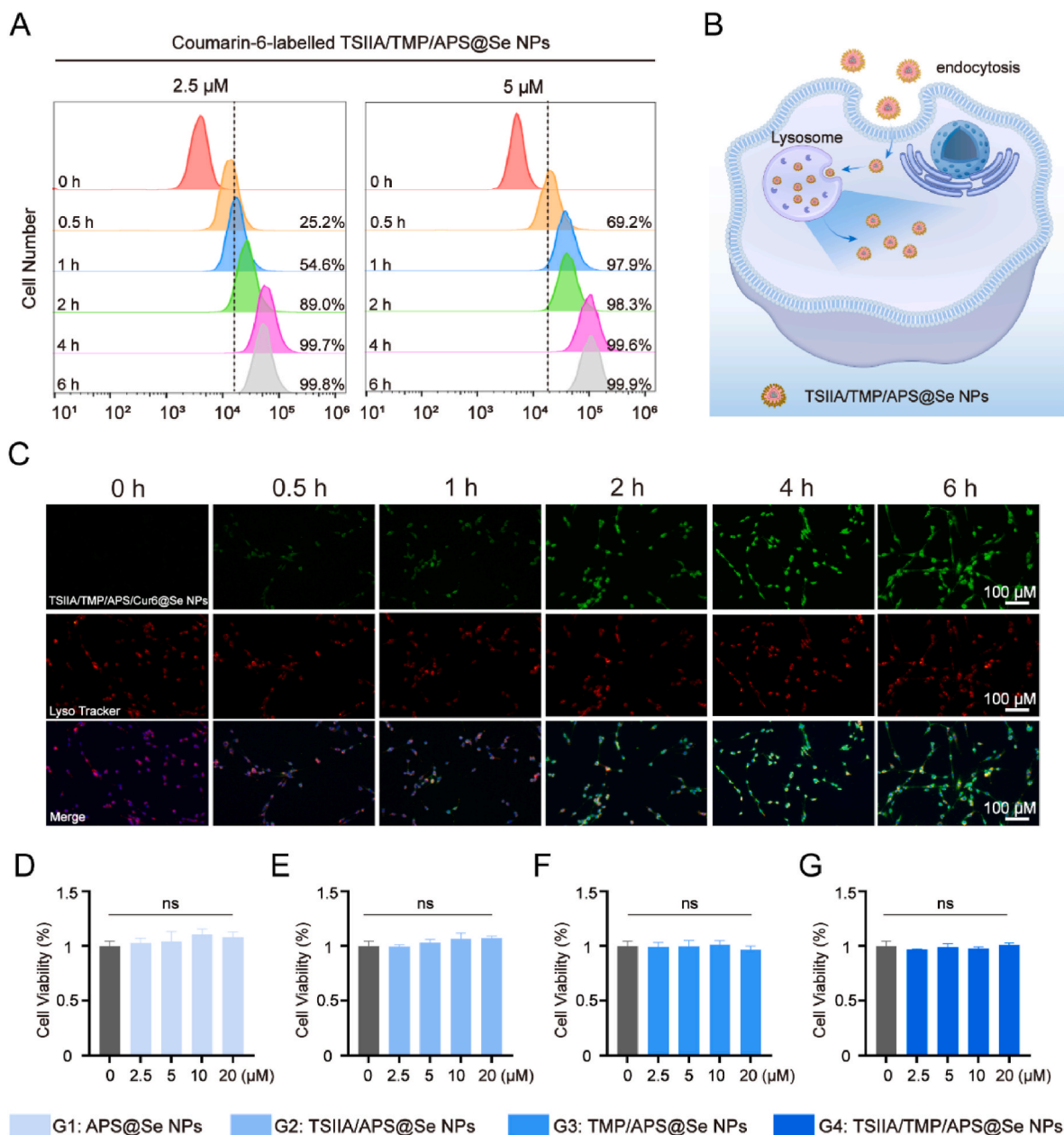
Fig. 2. Cellular uptake and intracellular trafficking of TSIIA/TMP/APS@Se NPs. (A) The fluorescence intensity of coumarin-6-labelled TSIIA/TMP/APS@Se NPs in PC12 cells for different time points was assessed by flow cytometry. (B) Schematic representation of the cellular internalization and intracellular release of TSIIA/TMP/APS@Se NPs in PC12 cells. (C) The visualization of cellular trafficking was achieved by using coumarin-6-labelled TSIIA/TMP/APS@Se NPs in PC12 cells, with DAPI (blue, nucleus) and lysotracker (red, lysosome) staining, Scale bar = 100 μm. (D–G) Cytotoxicity of (D) APS@Se NPs, (E) TSIIA/APS@Se NPs, (F) TMP/APS@Se NPs, and (G) TSIIA/TMP/APS@Se NPs in PC12 cells at different concentrations for 24 h of incubation. ns ($P > 0.05$) indicated no statistical difference. (For interpretation of the references to color in this figure legend, the reader is referred to the Web version of this article.)

(Fig. S2A). Due to the significant inhibitory effect of TSIIA on ferroptosis [30], the Se NPs decorated with TSIIA exhibited a superior anti-ferroptosis effect compared to Se NPs without TSIIA. Both TSIIA/TMP/APS@Se NPs and TSIIA/APS@Se NPs exhibited a protective effect against erastin-induced ferroptosis compared to TMP/APS@Se NPs and APS@Se NPs at equivalent therapeutic concentrations of 5 μM and 10 μM, with TSIIA/TMP/APS@Se NPs demonstrating superior inhibitory effects (Fig. 3A and B). Based on these results, we determined that a concentration of 5 μM is optimal for subsequent experiments. In addition to the significant decrease in cellular viability, ferroptosis is characterized by excessive accumulation of Fe^{2+}, overproduction of ROS.

Exacerbation of lipid peroxidation, and depletion of antioxidant defenses [55]. To further investigate the resistance of TCM-based ingredients to ferroptosis when incorporated into selenium-based composite nanocarriers, PC12 cells were initially cultured with APS@Se NPs, TSIIA/APS@Se NPs, TMP/APS@Se NPs, and TSIIA/TMP/APS@Se NPs for 2 h, followed by the addition of erastin to the medium for an additional 24 h. To visualize intercellular Fe^{2+} levels and quantify the total iron content in PC12 cells, we employed the FerroOrange fluorescence probe and a cell total iron colorimetric assay kit. Results obtained from confocal laser scanning microscopy (CLSM) demonstrated that the erastin group exhibited strong orange fluorescence compared to the control group, indicating increased accumulation of Fe^{2+} (Fig. 3C and Fig. S2B). The fluorescence emission intensity of FerroOrange was significantly reduced following treatment with TSIIA/TMP/APS@Se
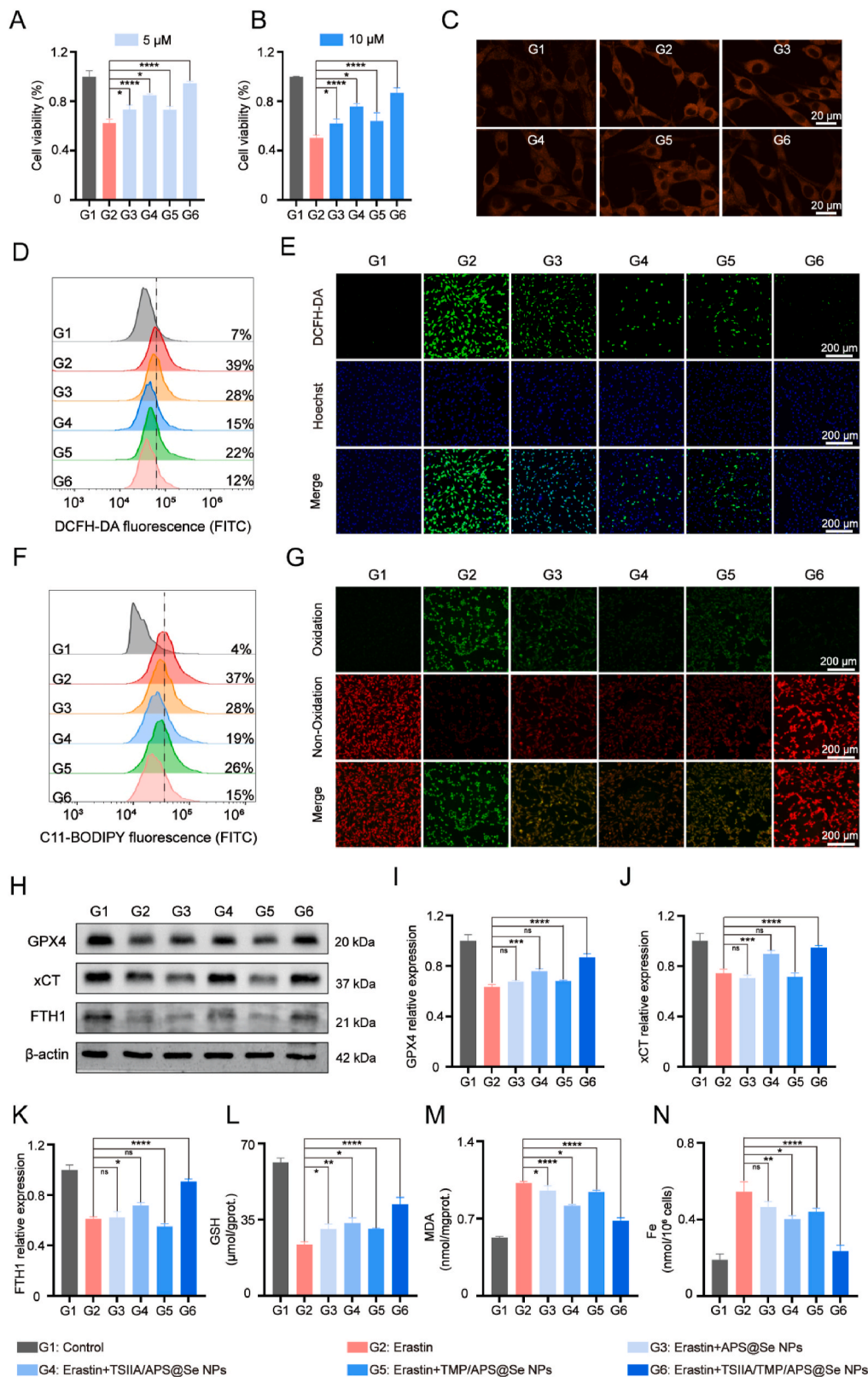
Fig. 3. TSIIA/TMP/APS@Se NPs protect PC12 cells from ferroptosis *in vitro*. (A, B) The CCK-8 results of PC12 cells co-cultured with erastin (750 nM) and nanoparticles (APS@Se NPs, TSIIA/APS@Se NPs, TMP/APS@Se NPs, and TSIIA/TMP/APS@Se NPs) at (A) 5 μM and (B) 10 μM for 24 h. (C) The representative images of Fe^{2+} in PC12 cells with FerroOrange staining; Scale bar = 20 μm. (D) Flow cytometry result of the relative fluorescence intensities of PC12 cells after incubation with DCFH-DA probe. (E) The representative images of PC12 cells were stained with a DCFH-DA probe. Scale bar = 200 μm. (F) Flow cytometry result of the relative fluorescence intensities of PC12 cells after incubation with BODIPY C11 probe. (G) The representative images of PC12 cells stained with BODIPY C11 probe. Scale bar = 200 μm. (H) Protein expression images of GPX4, xCT, and FTH1 in PC12 cells after different treatments of nanoparticles. (I–K) The quantitative analysis of protein of (I) GPX4, (J) xCT, and (K) FTH1 after different treatments of nanoparticles. (L–N) The quantitative analysis of (L) GSH, (M) MDA, and (N) total iron level in PC12 cells after different treatments of nanoparticles. *$P < 0.05$, **$P < 0.01$, ***$P < 0.001$, ****$P < 0.0001$, and ns ($P > 0.05$) suggested no statistical difference.

NPs and TSIIA/APS@Se NPs. In contrast, treatments with APS@Se NPs and TMP/APS@Se NPs showed comparatively lower efficacy. Additionally, the results of the cell total iron assessment corroborated the findings from the FerroOrange test (Fig. 3N). The overproduction of ROS, resulting from the initiation of the Fenton reaction triggered by the accumulation of iron reacting with hydrogen peroxide, serves as a critical indicator of ferroptosis. The ROS-scavenging capacity of the developed Se NPs in PC12 cells was assessed using 2′,7′-dichlorodihydrofluorescein diacetate (DCFH-DA) staining, a ROS-sensitive fluorescent probe. This probe produces green fluorescence that can be detected by flow

Cytometry and fluorescence microscopy. As shown in Fig. 3D, the level of ROS in PC12 cells increased to 39 % following erastin treatment, compared to 7 % in the control group. Interestingly, the increase in intracellular ROS was significantly suppressed by TSIIA/TMP/APS@Se NPs and TSIIA/APS@Se NPs, reducing ROS levels to 12 % and 15 %, respectively. Representative fluorescence images of PC12 cells further confirmed

These results, showing that the enhanced green fluorescence intensity caused by erastin was notably diminished after incubation with TSIIA/TMP/APS@Se NPs and TSIIA/APS@Se NPs (Fig. 3E and Fig. S2C) [56]. Subsequently, ROS interacts with the side chains of polyunsaturated fatty acids, facilitating the formation of lipid peroxidation products such as MDA and 4-HNE. This process accelerates lipid peroxidation, ultimately inducing ferroptosis [57]. To assess lipid peroxidation levels in PC12 cells, we employed the BODIPY 581/591C11 probe and an MDA assay kit. After erastin treatment, we observed a 33 % increase in C11 fluorescence intensity in PC12 cells compared to the control group. This increase was reversed, with fluorescence intensity declining to 15 % following the administration of TSIIA/TMP/APS@Se NPs. Similar trends were noted in the TSIIA/APS@Se NPs group. However, the APS@Se NPs and TMP/APS@Se NPs groups exhibited a weaker ability to reduce the fluorescence intensity caused by erastin (Fig. 3F). Fluorescence images and quantification of the BODIPY 581/591C11 probe corroborated these findings (Fig. 3G and Fig. S2D). The erastin-treated PC12 cells exhibited heightened lipid oxidation, while APS@Se NPs and TMP/APS@Se NPs displayed only mild antioxidative effects. In contrast, TSIIA/APS@Se NPs and TSIIA/TMP/APS@Se NPs significantly shifted the status from oxidative to non-oxidative, with TSIIA/TMP/APS@Se NPs demonstrating the most pronounced therapeutic effect (Fig. 3G). Our findings indicated that exposure to erastin induces lipid peroxidation in PC12 cells, while Se NPs loaded with TSIIA effectively decrease lipid peroxidation levels, alleviating ferroptosis in these cells. Analysis of MDA content in PC12 cells revealed similar results. MDA levels were elevated in the erastin group, while TSIIA/TMP/APS@Se NPs and TSIIA/APS@Se NPs exhibited a downregulating effect on MDA levels (Fig. 3M). The system Xc-, composed of GSH and GPX4, serves as the primary mechanism for cellular defense against ferroptosis. Evaluating the protein levels of GSH and GPX4 is an effective method for assessing ferroptosis [58]. Additionally, autophagy-dependent ferroptosis leads to decreased levels of ferritin heavy chain 1 (FTH1) due to autophagy activation, which facilitates ferritin degradation [59]. Western blot analysis revealed a reduction in the expression of GPX4, xCT, and FTH1 in PC12 cells following treatment with erastin. In contrast, their expression was upregulated after intervention with various Se NPs, particularly with TSIIA/APS@Se NPs and TSIIA/TMP/APS@Se NPs (Fig. 3H-K). Moreover, GSH, an antioxidant [60,61], was found to be depleted in erastin-induced PC12 cells. However, TSIIA/TMP/APS@Se NPs and TSIIA/APS@Se NPs were effective in rescuing GSH levels compared to APS@Se NPs and TMP/APS@Se NPs (Fig. 3L). These results indicated that PC12 cells undergoing ferroptosis exhibited a reduced survival rate, excessive accumulation of Fe^{2+}, increased levels of ROS, heightened lipid peroxidation, and depletion of antioxidant defenses. In contrast, TSIIA/TMP/APS@Se NPs and TSIIA/APS@Se NPs demonstrated effective resistance against ferroptosis.

3.4. TSIIA/TMP/APS@Se NPs enhance mitochondrial function to protect PC12 cells from ferroptosis

Mitochondria play a crucial role in the generation of ROS. The aforementioned results indicated a significant accumulation of ROS in PC12 cells, suggesting the potential for mitochondrial dysfunction [62, 63]. To validate the efficacy of TSIIA/TMP/APS@Se NPs, we further investigated the mitochondrial microstructure and function. TEM was employed to observe alterations in mitochondrial microstructure across different groups. As expected, erastin treatment resulted in significant mitochondrial shrinkage and reduced cristae density in PC12 cells, which.

are characteristic changes associated with ferroptosis. Notably, TSIIA/TMP/APS@Se NPs partially restored the primary cristae and membrane density structure in mitochondria, demonstrating superior therapeutic effects (Fig. 4A). The balanced distribution of charge across the inner mitochondrial membrane is crucial for maintaining mitochondrial function, commonly referred to as MMP [64]. JC-1 is a fluorescent dye used to detect MMP; it emits red fluorescence from J-aggregates during hyperpolarization and green fluorescence from J-monomers during depolarization [65]. These changes can be quantified by measuring the red and green fluorescence signals using flow cytometry and fluorescence imaging, facilitating the assessment of mitochondrial functionality (Fig. 4B). As shown in Fig. 4C and D, the percentage of JC-1 monomers associated with polarized mitochondria decreased significantly from 59.6 % to 20.3 % in the TSIIA/TMP/APS@Se NPs group. TSIIA/APS@Se NPs reduced the green fluorescence intensity from 59.6 % to 33.6 %, while the TMP/APS@Se NPs and APS@Se NPs groups maintained relatively strong fluorescence levels similar to those observed in the erastin group. The flow cytometric results were validated by visualizing cell images using a fluorescence microscope. The decrease in red fluorescence and the increase in green fluorescence following erastin treatment were mitigated by co-culturing with TSIIA/TMP/APS@Se NPs and TSIIA/APS@Se NPs, as indicated in the quantitative analysis of fluorescence intensity presented in Figs. S2E and S2F. This indicated that both TSIIA/TMP/APS@Se NPs and TSIIA/APS@Se NPs can restore MMP and help resist ferroptosis (Fig. 4E).

3.5. TSIIA/TMP/APS@Se NPs upregulate M2 microglial polarization and downregulated M1 polarization to attenuate inflammation in vitro

The immortalized murine microglial cell line BV2 is commonly used as a surrogate for primary microglia in CNS research [66]. Activated microglia, particularly the M1 phenotype, play a pivotal role in initiating inflammatory responses by releasing inflammatory mediators such as TNF-α, IL-6, and IL-1β [67]. In this study, BV2 cells were treated with lipopolysaccharide (LPS) at a concentration of 1 μg/mL for 10 h to induce an inflammatory environment and validate the anti-inflammatory potential of.

Various TCM-based Se NPs. Following LPS treatment, the levels of inflammatory cytokines, including IL-6, IL-1β, and TNF-α, significantly increased, while the secretion of the anti-inflammatory factor IL-10 decreased. The upregulation of these inflammatory cytokines indicated the successful establishment of the inflammatory model. Notably, BV2 cells treated with TSIIA/TMP/APS@Se NPs and TMP/APS@Se NPs exhibited a significant reduction in inflammatory cytokines (TNF-α, IL-1β, and IL-6) and an enhancement in the levels of the anti-inflammatory factor IL-10 compared to those treated with TSIIA/APS@Se NPs and APS@Se NPs (Fig. 5A-D). Furthermore, the state of the spinal cord tissue microenvironment is primarily influenced by the polarization of microglia [68] (Fig. 5E). Consistent with this, western blot analysis revealed a marked increase in the levels of the M1 marker iNOS and a decrease in the M2 marker Arg-1 following LPS treatment (Fig. 5F). Both the TSIIA/TMP/APS@Se NPs and TMP/APS@Se NPs groups demonstrated a reversal of these effects under pathological conditions, as
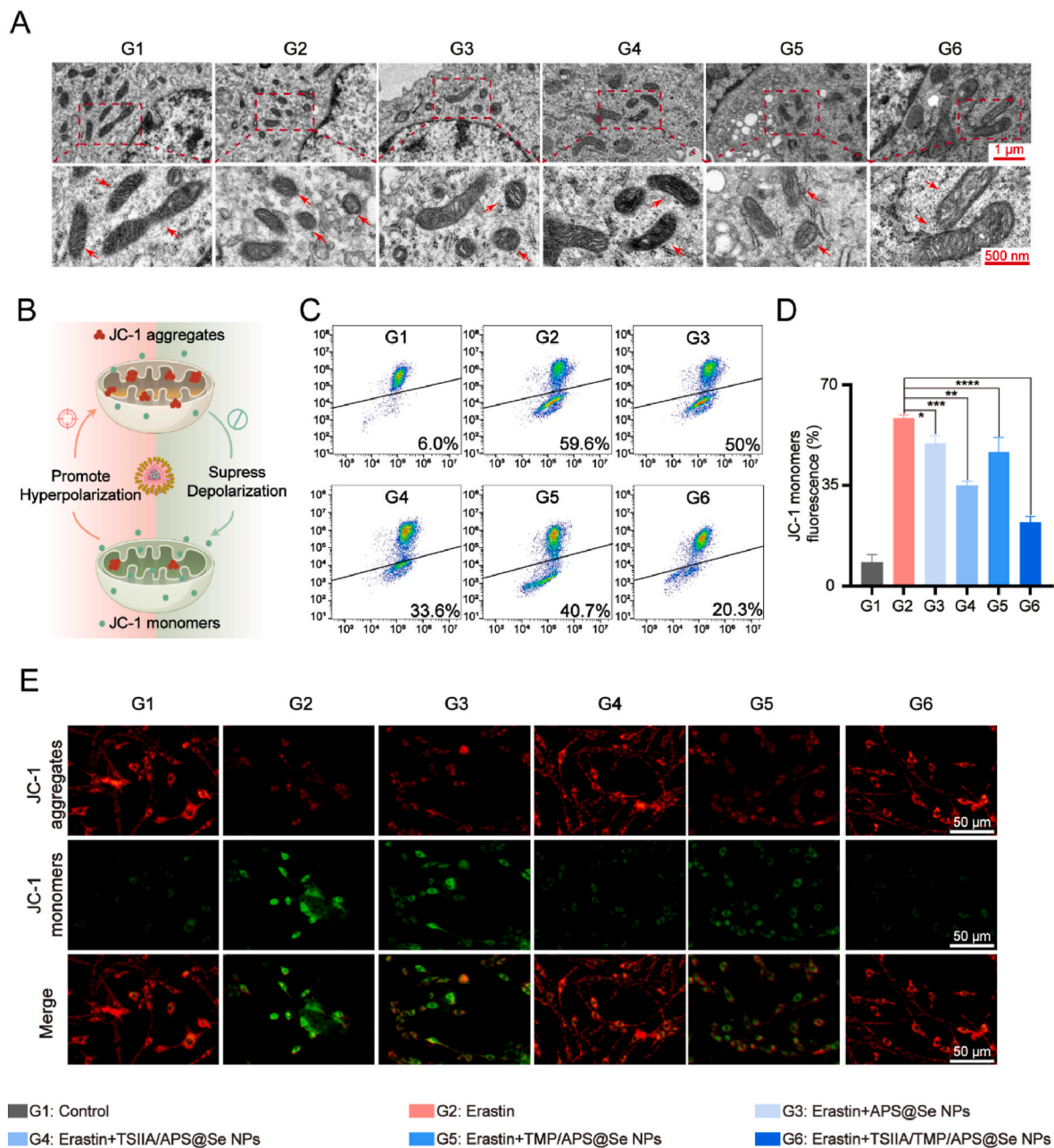
Fig. 4. TSIIA/TMP/APS@Se NPs resist ferroptosis by modulating mitochondrial functions in PC12 cells. (A) The representative mitochondria TEM images of PC12 cells after different treatments of nanoparticles. The red arrow indicates mitochondria. Scale bars = 1 μm and 500 nm, respectively. (B) Schematic illustration of mitochondrial membrane potential change of mitochondria after the treatment of TSIIA/TMP/APS@Se NPs. (C) Flow cytometry results of the relative fluorescence intensities of PC12 cells after incubation with JC-1 probe. (D) The quantitative analysis of JC-1 monomers fluorescence intensity in PC12 cells after treatments with different nanoparticles. (E) The representative images of the JC-1 probe of PC12 cells after treatment with different nanoparticles. Scale bar = 50 μm *$P < 0.05$, **$P < 0.01$, ***$P < 0.001$, ****$P < 0.0001$, and ns ($P > 0.05$) suggested no statistical difference. (For interpretation of the references to color in this figure legend, the reader is referred to the Web version of this article.)

indicated by decreased iNOS levels and increased Arg-1 levels (Fig. 5F, Figs. S3A and S3B). Furthermore, flow cytometry analysis revealed a drastic increase in the M1 phenotype (CD16/32 and F4/80 dual positive) and a minor reduction in the M2 phenotype (CD206 and F4/80 dual positive) in BV2 stimulated with LPS. After treatment with TSIIA/TMP/APS@Se NPs, there was a noticeable decrease in the fluorescence intensity of the M1 phenotype, while the M2 phenotype exhibited an increase in fluorescence intensity. A similar observation was noted in the TMP/APS@Se NPs group, indicating that TMP-decorated nanocarriers prevented the polarization of microglia towards the M1 phenotype, promoted their transition to the M2

phenotype, and mitigated the inflammatory microenvironment (Fig. 5G).

3.6. TSIIA/TMP/APS@Se NPs protect neuronal cell death against microglia activation

Neuronal destruction in SCI has been associated with the pro-inflammatory activation of microglia [69]. To further confirm the effect of microglial activation on neurons and validate the efficacy of TSIIA/TMP/APS@Se NPs, *in vitro* experiments were conducted using a co-culture model system comprising PC12 cells and LPS-induced BV2
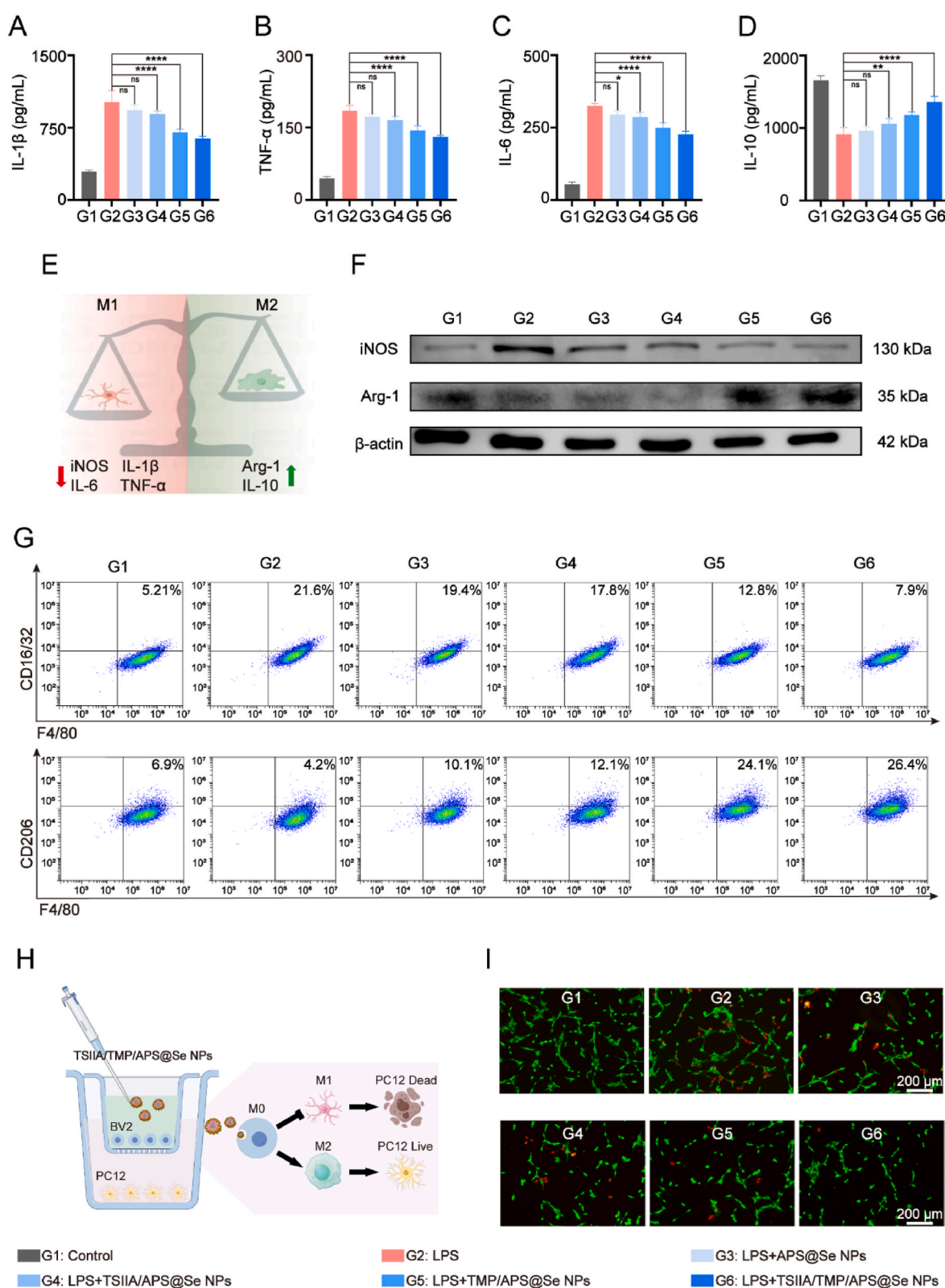
Fig. 5. TSIIA/TMP/APS@Se NPs regulate the polarization of BV2 cells and improve the inflammatory microenvironment to rescue PC12 cells in a co-culture system. (A–D) The ELISA quantitative analysis of the inflammatory cytokines in BV2 cells after different treatments. (E) Schematic illustration of the modulation of TSIIA/TMP/APS@Se NPs on BV2 polarization. (F) Protein expression images of iNOS and Arg-1 in BV2 cells after different treatment of nanoparticles. (G) Flow cytometry result of the BV2 cells to identify the M1 phenotype (F4/80, CD16/32 double positive) and M2 phenotype (F4/80, CD206 double positive) after incubation with F4/80, CD16/32, CD206. (H) Schematic illustration of a co-cultured system between PC12 cells and BV2 cells, indicating outcomes of diverse treatments with Se NPs. (I) The representative images of Live/Dead stains of PC12 cells after different treatments of the co-cultured system. Scale bar = 200 μm *$P < 0.05$, **$P < 0.01$, ***$P < 0.001$, ****$P < 0.0001$, and ns ($P > 0.05$) suggested no statistical difference.

cells. The BV2 cells were initially seeded in the upper compartment for 12 h, after which the PC12 cells were added to the lower chamber. Following adherence, the BV2 cells were co-incubated with APS@Se NPs, TSIIA/APS@Se NPs, TMP/APS@Se NPs, and TSIIA/TMP/APS@Se

NPs for 2 h. Subsequently, an LPS-containing medium (1 μg/mL) was added to the upper chamber for an additional 10 h. After the PC12 cells adhered, the pretreated BV2 cells were transferred from the upper compartment to the lower compartment of the Transwell system and
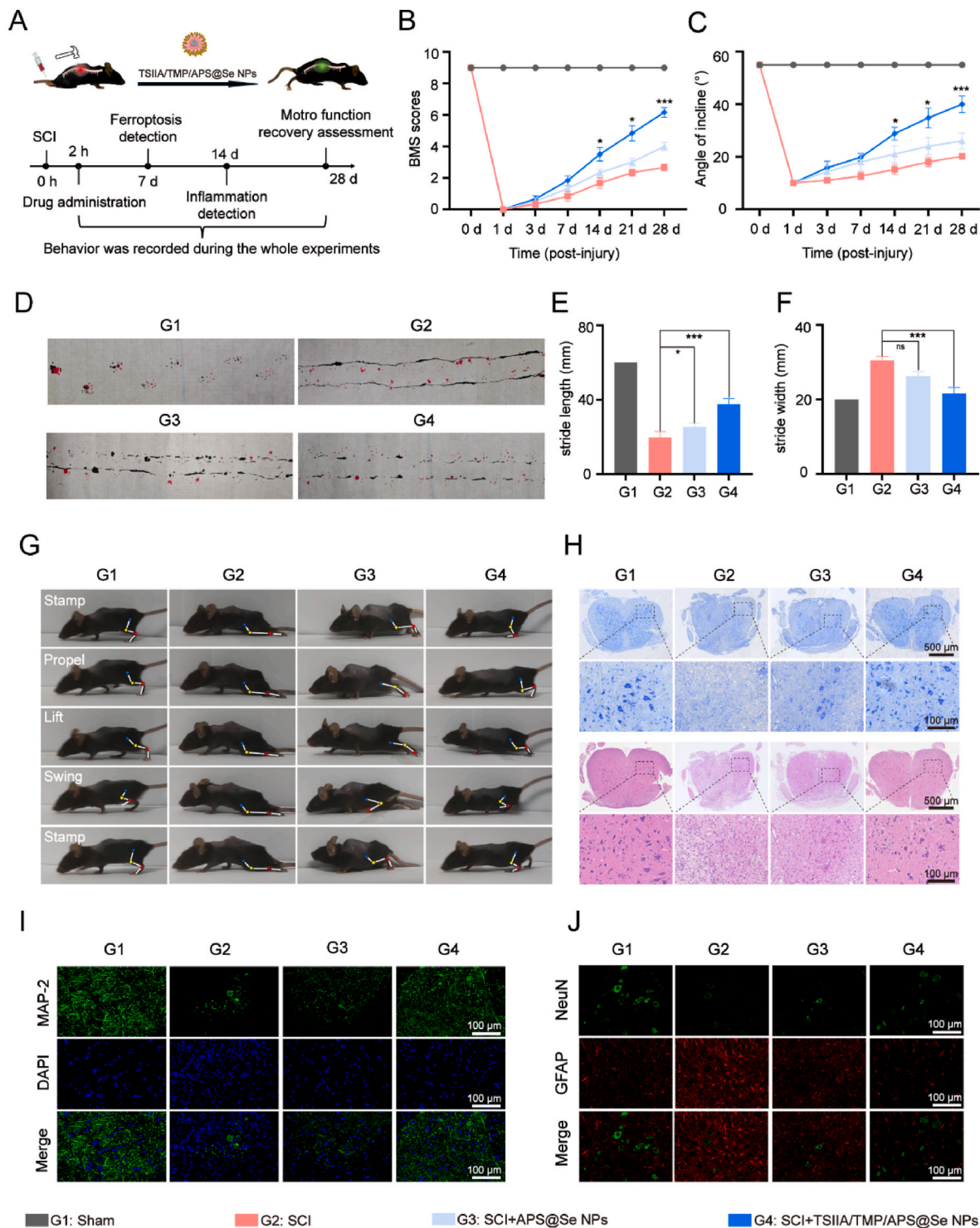

Fig. 6. The *in vivo* validation of the internal therapeutic effects and functional outcome recovery of TSIIA/TMP/APS@Se NPs. (A) Schematic illustration of the entire animal experiment treatment in the SCI model. (B–G) Motor function recovery was measured by (B) BMS score, (C) angle of incline, (D) represented footprints marked with red and black dyes, and (G) hindlimbs motion analysis. (E, F) The quantitative analysis of the footprints experiment includes measuring the (E) stride length and (F) stride width of mice after different treatments. (H) H&E staining and Nissl staining. (I) The representative immunofluorescence images of MAP-2 staining in the spinal cord tissue of mice subjected to various treatments. Scale bar = 100 μm. (J) The representative immunofluorescence images of GFAP and NeuN staining in the spinal cord tissue of mice subjected to different treatments. Scale bar = 100 μm $*P < 0.05$, $***P < 0.001$, and ns ($P > 0.05$) suggested no statistical difference. (For interpretation of the references to color in this figure legend, the reader is referred to the Web version of this article.)

incubated for 24 h (Fig. 5H). The Live/Dead assay revealed a significant increase in the red fluorescence intensity of PC12 cells co-incubated with LPS-activated BV2 cells. In contrast, the TSIIA/TMP/APS@Se NPs groups exhibited prominent green fluorescence and reduced red fluorescence in the PC12 cells. A similar trend was observed in the TMP/APS@Se NPs groups (Fig. 5I, Figs. S3C and S3D). Furthermore, flow cytometric analysis demonstrated that the total cell death rate of PC12 cells was 27.21 % in the LPS treatment group. However, this rate declined to 13.29 % in the TSIIA/TMP/APS@Se NPs group and 17.04 % in the TMP/APS@Se NPs group (Fig. S4). Collectively, these results indicated that microglial activation exacerbates neuronal death, while TSIIA/TMP/APS@Se NPs effectively counteract this phenomenon.

3.7. TSIIA/TMP/APS@Se NPs facilitate the motor function of mice post-SCI

Based on the promising capacity of TSIIA/TMP/APS@Se NPs to inhibit ferroptosis and their remarkable ability to remodel inflammation demonstrated *in vitro*, we proceeded to validate their internal therapeutic effects and functional recovery outcomes in a T10 spinal cord contusion mouse model. The entire experimental schedule was conducted according to the details outlined in Fig. 6A. During the 28-day.

Therapy period following SCI, we performed a comprehensive assessment of motor function recovery, utilizing simultaneous measurements of the basso mouse scale (BMS), inclined plane test, footprint analysis, and hindlimbs motion analysis. Mice in all groups, except those in the sham group, exhibited an immediate loss of hindlimbs motor function following the SCI operation, as indicated by a BMS score of 0. A gradual improvement in BMS scores was observed across all groups over time. Notably, the TSIIA/TMP/APS@Se NPs group demonstrated significantly higher scores on 14th day, 21th day, and 28th day post-surgery, indicating a faster restoration of hindlimbs locomotion. In contrast, SCI mice injected with PBS displayed limited self-healing performance, with average BMS scores not exceeding 4 on 28th day (Fig. 6B). Consistently, mice treated with TSIIA/TMP/APS@Se NPs also showed an enhanced angle of incline compared to the SCI group (Fig. 6C). Additionally, footprint analysis yielded similar results; mice receiving TSIIA/TMP/APS@Se NPs injection exhibited coordinated hindlimbs gaits characterized by longer stride length and shorter stride width. In contrast, mice in the SCI group displayed dragging gaits with short stride length and wide stride width (Fig. 6D-F). The motion of the hindlimbs during walking was visualized and can be divided into a series of events: stamping, propelling, lifting, swinging, and returning to stamping, thus completing a cycle. As shown in Fig. 6G, the mice in the SCI group exhibited paralysis and maintained a dragging gait throughout the entire cycle. In contrast, the mice treated with TSIIA/TMP/APS@Se NPs demonstrated remarkable improvements in their gait cycle, including restored standing posture, increased iliac crest height, and enhanced joint range of motion. These findings strongly suggested the outstanding therapeutic effects of TSIIA/TMP/APS@Se NPs, which improved hindlimbs strength, restored the gait cycle, and facilitated the recovery of hindlimbs function. Subsequently, H&E staining and Nissl staining were performed to elucidate the histological pathology and structural alterations in spinal cord tissue of mice subjected to various treatments after SCI. H&E staining revealed an intact tissue structure and normal morphology of the spinal cord in the sham group, characterized by evenly distributed neuronal cells and distinct nucleoli. In contrast, the SCI group exhibited significant disorganization of gray matter, pronounced necrosis and cavitation, irregular neuronal morphology with pyknotic nuclei, and substantial loss of motor neurons. However, treatment with TSIIA/TMP/APS@Se NPs mitigated these pathological impairments (Fig. 6H). The results from Nissl staining were consistent with those from H&E staining, showing better preservation of Nissl-positive neurons at the lesion site in the TSIIA/TMP/APS@Se NPs treatment group compared to the SCI group (Fig. 6H). Additionally, axonal regeneration was examined through immunofluorescence

staining of harvested tissues with MAP-2, a recognized marker of axonal regeneration. The density of MAP-2 was significantly reduced in spinal tissue following contusive injury. However, fluorescence levels of MAP-2 were restored in the TSIIA/TMP/APS@Se NPs treatment group (Fig. 6I and Fig. S5A). A similar outcome was observed in NF-200 immunofluorescence analysis, indicating that axonal regeneration occurred with treatment using TSIIA/TMP/APS@Se NPs (Figs. S5B and S6). The revival of neurons and the formation of astrocyte derived glial scars play a crucial role in influencing the rehabilitation of SCI [7,70]. As shown in Fig. 6J, the NeuN-positive signal was significantly stronger in the sham group compared to the SCI group, while the glial fibrillary acidic protein (GFAP) positive fluorescence was weaker in the sham group. As expected, the TSIIA/TMP/APS@Se NPs group demonstrated a remarkable ability to enhance the recovery of NeuN-positive signals while attenuating the generation of GFAP-positive signals (Fig. 6J). The quantification of NeuN and GFAP fluorescence results is depicted in Figs. S5C and S5D. These findings provided strong evidence for the extraordinary neuroprotective effects of TSIIA/TMP/APS@Se NPs in enhancing motor function recovery by reducing neuronal damage, promoting axon regeneration, and attenuating glial scar formation in mice with SCI.

3.8. In vivo ferroptosis resistance effects of TSIIA/TMP/APS@Se NPs

After confirming the effectiveness of TSIIA/TMP/APS@Se NPs in promoting motor function recovery and facilitating tissue repair, our subsequent investigation focused on elucidating the underlying mechanisms contributing to their therapeutic efficacy. Increasing evidence has demonstrated a close correlation between ferroptosis and the secondary injury associated with SCI [71]. Consistent with the results of the *in vitro*

Experiments, we observed downregulation of GPX4 and xCT expression in mice with SCI. This trend was reversed by the administration of TSIIA/TMP/APS@Se NPs, indicating that ferroptosis was effectively mitigated through the application of these TCM-based Se NPs (Fig. 7A-C). This finding was further supported by immunofluorescence results, which showed a significant decrease in both the number of neurons and the level of GPX4 following SCI. However, this phenomenon was reversed after treatment with TSIIA/TMP/APS@Se NPs (Fig. 7D, Figs. S7A and S7B). Similarly, 4-HNE, a marker of lipid peroxidation, exhibited strong fluorescence after SCI. However, treatment with TSIIA/TMP/APS@Se NPs reduced lipid peroxidation levels, thereby preserving neuronal integrity (Fig. 7E, Figs. S7C and S7D). Collectively, these findings demonstrated that ferroptosis occurs in the SCI mouse model and that TCM-based nanoparticles can effectively counteract this process.

3.9. TSIIA/TMP/APS@Se NPs regulate microglial polarization and inflammatory responses in vivo

Our study confirmed the capacity of TSIIA/TMP/APS@Se NPs to alter polarization states and demonstrated their outstanding anti-inflammatory efficacy in BV2 cells under LPS-induced inflammatory conditions. Consequently, further investigation is required to assess their biological therapeutic effects *in vivo*. As shown in Fig. 7F and G, the CD86 positive fluorescence intensity in the SCI group was significantly higher than that in the TSIIA/TMP/APS@Se NPs group (Fig. 7F). The quantification of fluorescence is presented in the image results (Fig. S7E). Additionally, CD86 positive cells were co-localized with Iba-1. Furthermore, the fluorescence intensity of CD206 was elevated after co-localization with Iba-1 in the TSIIA/TMP/APS@Se NPs group compared to the SCI group (Fig. 7G and Fig. S7F). Western blot analysis showed similar results, indicating that treatment with TSIIA/TMP/APS@Se NPs could suppress iNOS expression while promoting Arg-1 expression following SCI (Fig. 7H-I). Moreover, the release of pro-inflammatory cytokines was observed in this study. ELISA results demonstrated that levels of TNF-α, IL-6, and IL-1β were significantly
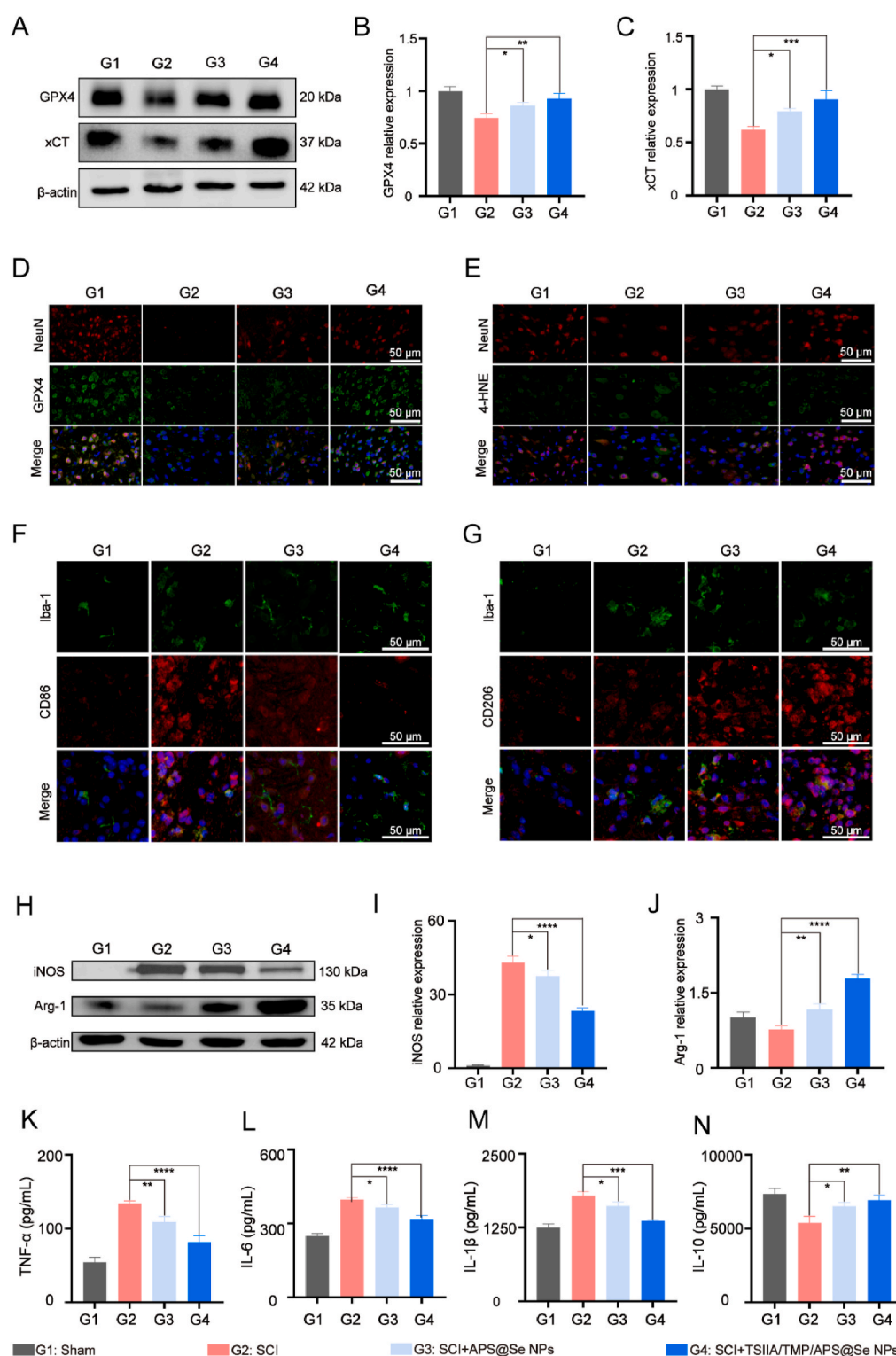
Fig. 7. The validation of the anti-ferroptosis and regulation of microglial polarization and improving inflammatory microenvironment capacity of TSIIA/TMP/APS@Se NPs *in vivo*. (A) Protein expression images of GPX4, xCT in the spinal cord tissue of mice after different treatment of nanoparticles. (B, C) The quantitative analysis of protein of (B) GPX4, and (C) xCT after different treatment of nanoparticles. (D) The representative immunofluorescence images of GPX4 and NeuN staining in the spinal cord tissue of mice subjected to different treatments. Scale bar = 50 μm. (E) The representative immunofluorescence images of 4-HNE and NeuN staining in the spinal cord tissue of mice subjected to different treatments. Scale bar = 50 μm. (F, G) The representative immunofluorescence images of Iba-1, (F) CD86, and (G) CD206 co-staining in the spinal cord tissue of mice subjected to different treatments. Scale bar = 50 μm. (H) Protein expression images of iNOS, Arg-1 in the spinal cord tissue of mice after different treatments of nanoparticles. (I, J) Quantitative analysis of protein of (I) iNOS and (J) Arg-1 after different treatments of nanoparticles. (K–N) The quantitative analysis of the inflammatory cytokines in spinal cord tissue of mice after different treatments using ELISA. $*P < 0.05$, $**P < 0.01$, $***P < 0.001$, $****P < 0.0001$, and ns ($P > 0.05$) suggested no statistical difference.

increased in the SCI group, while IL-10 levels decreased. As expected, these pro-inflammatory cytokines were substantially downregulated after therapy, particularly following the administration of TSIIA/TMP/APS@Se NPs (Fig. 7K-N). These results indicated that TSIIA/TMP/APS@Se NPs can enhance M2 polarization while suppressing M1 polarization, thereby modulating the microenvironment to mitigate inflammatory injury in the spinal cord.

4. Conclusion

In this study, we successfully synthesized an innovative delivery platform of TSIIA/TMP/APS@Se NPs by employing Se NPs functionalized with APS and loaded with TSIIA and TMP, guided by the principles of TCM compatibility theory. This groundbreaking design not only enhances the bioavailability of APS, TSIIA, and TMP, but also provides a highly stable, long-acting, and efficient delivery system to effectively facilitate the anti-ferroptosis and anti-inflammation functions of their properties. Encouragingly the TSIIA/TMP/APS@Se NPs exhibited remarkable anti-ferroptosis by inhibiting iron deposition, mitigating lipid peroxidation, rescuing system Xc-system and recovering mitochondrial *in vitro*. Moreover, the TSIIA/TMP/APS@Se NPs demonstrated extraordinary anti-inflammatory capacities by regulating the polarization states as well. These concurrent modulations ultimately facilitated the functional restoration of SCI mice in the *in vivo* experiment we conducted, enhancing neuronal recovery, promoting axonal regeneration, and alleviating glial scar formation. Collectively, these findings suggest that TSIIA/TMP/APS@Se NPs represent a promising therapeutic strategy for SCI, marking a significant advancement in the development of synergistic drugs from TCM active ingredients using nanotechnology.

CRediT authorship contribution statement

Luoqi Mai: Writing – original draft, Supervision, Methodology, Investigation, Data curation, Conceptualization. **Jinggong Liu:** Writing – review & editing, Validation, Supervision, Project administration, Investigation, Data curation, Conceptualization. **Huimei Wu:** Writing – review & editing, Supervision, Methodology, Data curation. **Hongshen Wang:** Validation, Project administration, Methodology, Data curation. **Zhidong Lin:** Validation, Project administration, Methodology. **Siyuan Rao:** Validation, Software, Formal analysis. **Wenxi Sun:** Resources, Formal analysis. **Aowei Tan:** Resources, Formal analysis. **Yongpeng Lin:** Writing – review & editing, Software, Resources, Project administration, Methodology, Funding acquisition, Formal analysis, Conceptualization. **Bolai Chen:** Writing – review & editing, Visualization, Validation, Supervision, Project administration, Investigation, Funding acquisition, Data curation, Conceptualization.

Declaration of generative AI and AI-assisted technologies in the writing process

During the preparation of this work, the author used the Youdao Dictionary AI tool to polish this article. After using this tool, the author reviewed and edited the content as needed and took full responsibility for the content of the publication.

Declaration of competing interest

The authors declare no conflict of interest.

Acknowledgments

Appendix A. Supplementary data

Supplementary data to this article can be found online at https://doi.org/10.1016/j.mtbio.2025.101758.

Data availability

Data will be made available on request.

References

[1] J.A.G. Crispo, L.K. Kuramoto, J.J. Cragg, Global burden of spinal cord injury: future directions, Lancet Neurol. 22 (2023) 976–978.

[2] J. Meng, J. Sun, J. Kang, S. Ren, M. Xu, R. Li, X. Zhao, Y. Yuan, L. Xin, R. Zhang, Multifunctional hydrogels loaded with tellurium nanozyme for spinal cord injury repair, Mater. Today Bio 29 (2024) 101339.

[3] G.S.C.I. Collaborators, Global, regional, and national burden of spinal cord injury, 1990-2019: a systematic analysis for the Global Burden of Disease Study 2019, Lancet Neurol. 22 (2023) 1026–1047.

[4] K.F. So, A comprehensive study of gene expression and molecular regulation following spinal cord injury, Engineering 6 (2020) 389–390.

[5] B. Zheng, M.H. Tuszynski, Regulation of axonal regeneration after mammalian spinal cord injury, Nat. Rev. Mol. Cell Biol. 24 (2023) 396–413.

[6] K. Shen, X. Li, G. Huang, Z. Yuan, B. Xie, T. Chen, L. He, High rapamycin-loaded hollow mesoporous Prussian blue nanozyme targets lesion area of spinal cord injury to recover locomotor function, Biomaterials 303 (2023) 122358.

[7] X. Hu, W. Xu, Y. Ren, Z. Wang, X. He, R. Huang, B. Ma, J. Zhao, R. Zhu, L. Cheng, Spinal cord injury: molecular mechanisms and therapeutic interventions, Signal Transduct. Targeted Ther. 8 (2023) 245.

[8] X. Zhao, X. Hu, W. Wang, S. Lu, Macrophages dying from ferroptosis promote microglia-mediated inflammatory responses during spinal cord injury, Int. Immunopharmacol. 143 (2024) 113281.

[9] X.Y. Bai, X.L. Liu, Z.Z. Deng, D.M. Wei, D. Zhang, H.L. Xi, Q.Y. Wang, M.Z. He, Y. L. Yang, Ferroptosis is a new therapeutic target for spinal cord injury, Front. Neurosci. 17 (2023) 1136143.

[10] J.Y. Han, Q. Li, K. Sun, C.S. Pan, J. Liu, P. Huang, J. Feng, Y.C. Liu, G.A. Meininger, Natural products improve organ microcirculation dysfunction following ischemia/reperfusion- and lipopolysaccharide-induced disturbances: mechanistic and therapeutic views, Engineering 38 (2024) 77–99.

[11] X. Jiang, B.R. Stockwell, M. Conrad, Ferroptosis: mechanisms, biology and role in disease, Nat. Rev. Mol. Cell Biol. 22 (2021) 266–282.

[12] S. Yao, M. Pang, Y. Wang, X. Wang, Y. Lin, Y. Lv, Z. Xie, J. Hou, C. Du, Y. Qiu, Y. Guan, B. Liu, J. Wang, A.P. Xiang, L. Rong, Mesenchymal stem cell attenuates spinal cord injury by inhibiting mitochondrial quality control-associated neuronal ferroptosis, Redox Biol. 67 (2023) 102871.

[13] N. Sumneang, N. Siri-Angkul, S. Kumfu, S.C. Chattipakorn, N. Chattipakorn, The effects of iron overload on mitochondrial function, mitochondrial dynamics, and ferroptosis in cardiomyocytes, Arch. Biochem. Biophys. 680 (2020) 108241.

[14] Y. Chen, S. Liu, J. Li, Z. Li, J. Quan, X. Liu, Y. Tang, B. Liu, The latest view on the mechanism of ferroptosis and its research progress in spinal cord injury, Oxid. Med. Cell. Longev. 2020 (2020) 6375938.

[15] M.H. Ge, H. Tian, L. Mao, D.Y. Li, J.Q. Lin, H.S. Hu, S.C. Huang, C.J. Zhang, X. F. Mei, Zinc attenuates ferroptosis and promotes functional recovery in contusion spinal cord injury by activating Nrf2/GPX4 defense pathway, CNS Neurosci. Ther. 27 (2021) 1023–1040.

[16] H. Geng, Z. Li, Z. Li, Y. Zhang, Z. Gao, L. Sun, X. Li, J. Cui, S. Ni, J. Hao, Restoring neuronal iron homeostasis revitalizes neurogenesis after spinal cord injury, Proc. Natl. Acad. Sci. U. S. A 120 (2023) e2220300120.

[17] A. Sierra, V.E. Miron, R.C. Paolicelli, R.M. Ransohoff, Microglia in health and diseases: integrative hubs of the central nervous system (CNS), Cold Spring Harbor Perspect. Biol. 16 (2024) a041366.

[18] Y. Long, X.Q. Li, J. Deng, Q.B. Ye, D. Li, Y. Ma, Y.Y. Wu, Y. Hu, X.F. He, J. Wen, A. Shi, S. Yu, L. Shen, Z. Ye, C. Zheng, N. Li, Modulating the polarization phenotype of microglia - a valuable strategy for central nervous system diseases, Ageing Res. Rev. 93 (2024) 102160.

[19] S.F. Darwish, A.M.M. Elbadry, A.S. Elbokhomy, G.A. Salama, R.M. Salama, The dual face of microglia (M1/M2) as a potential target in the protective effect of nutraceuticals against neurodegenerative diseases, Front. Aging 4 (2023) 1231706.

[20] R. Orihuela, C.A. McPherson, G.J. Harry, Microglial M1/M2 polarization and metabolic states, Br. J. Pharmacol. 173 (2016) 649–665.

[21] S. Guo, H. Wang, Y. Yin, Microglia polarization from M1 to M2 in neurodegenerative diseases, Front. Aging Neurosci. 14 (2022) 815347.

[22] J. Ren, B. Zhu, G. Gu, W. Zhang, J. Li, H. Wang, M. Wang, X. Song, Z. Wei, S. Feng, Schwann cell-derived exosomes containing MFG-E8 modify macrophage/ microglial polarization for attenuating inflammation via the SOCS3/STAT3 pathway after spinal cord injury, Cell Death Dis. 14 (2023) 70.

[23] G. Gu, B. Zhu, J. Ren, X. Song, B. Fan, H. Ding, J. Shang, H. Wu, J. Li, H. Wang, J. Li, Z. Wei, S. Feng, Ang-(1-7)/MasR axis promotes functional recovery after spinal cord injury by regulating microglia/macrophage polarization, Cell Biosci. 13 (2023) 23.

[24] H. Ma, C. Wang, L. Han, F. Kong, Z. Liu, B. Zhang, W. Chu, H. Wang, L. Wang, Q. Li, W. Peng, H. Yang, C. Han, X. Lu, Tofacitinib promotes functional recovery after spinal cord injury by regulating microglial polarization via JAK/STAT signaling pathway, Int. J. Biol. Sci. 19 (2023) 4865–4882.

[25] K. Shen, G. Sun, L. Chan, L. He, X. Li, S. Yang, B. Wang, H. Zhang, J. Huang, M. Chang, Z. Li, T. Chen, Anti-inflammatory nanotherapeutics by targeting matrix metalloproteinases for immunotherapy of spinal cord injury, Small 17 (2021) e2102102.

[26] W. Gong, T. Zhang, M. Che, Y. Wang, C. He, L. Liu, Z. Lv, C. Xiao, H. Wang, S. Zhang, Recent advances in nanomaterials for the treatment of spinal cord injury, Mater. Today Bio 18 (2023) 100524.

[27] Y. Xuan, K. Peng, R. Zhu, Y. Kang, Z. Yin, Hmox1 is identified as a ferroptosis hub gene and associated with the M1 type microglia/macrophage polarization in spinal cord injury: bioinformatics and experimental validation, Mol. Neurobiol. 60 (2023) 7151–7165.

[28] F. Zeng, A. Chen, W. Chen, S. Cheng, S. Lin, R. Mei, X. Mei, Knockout of TNF-α in microglia decreases ferroptosis and convert microglia phenotype after spinal cord injury, Heliyon 10 (2024) e36488.

[29] Y. Zhang, J.M. Ju, L. Jiao, B.F. Yang, Bioactive components of Chinese herbal medicines in the treatment of glucose and lipid metabolism disorders: evidence and potential mechanisms, Engineering 29 (2023) 73–82.

[30] T. Hu, H.X. Zou, S.Y. Le, Y.R. Wang, Y.M. Qiao, Y. Yuan, J.C. Liu, S.Q. Lai, H. Huang, Tanshinone IIA confers protection against myocardial ischemia/ reperfusion injury by inhibiting ferroptosis and apoptosis via VDAC1, Int. J. Mol. Med. 52 (2023) 109.

[31] P. Zhang, Q. Zhang, X. Liu, T. Li, S. Wu, Y. Li, Z. Jiang, Tanshinone protects against spinal cord ischemia-reperfusion injury by inhibiting JNK activity, Comput. Intell. Neurosci. 2022 (2022) 7619797.

[32] X. Feng, M. Li, Z. Lin, Y. Lu, Y. Zhuang, J. Lei, X. Liu, H. Zhao, Tetramethylpyrazine promotes axonal remodeling and modulates microglial polarization via JAK2-STAT1/3 and GSK3-NFκB pathways in ischemic stroke, Neurochem. Int. 170 (2023) 105607.

[33] Y. Chen, F. Peng, C. Yang, H. Hou, Z. Xing, J. Chen, L. Liu, C. Peng, D. Li, SIRT1 activation by 2,3,5,6-tetramethylpyrazine alleviates neuroinflammation via inhibiting M1 microglia polarization, Front. Immunol. 14 (2023) 1206513.

[34] Y. Rao, J. Li, R. Qiao, J. Luo, Y. Liu, Synergistic effects of tetramethylpyrazine and astragaloside IV on spinal cord injury via alteration of astrocyte A1/A2 polarization through the Sirt1-NF-κB pathway, Int. Immunopharmacol. 131 (2024) 111686.

[35] D.K. Anderson, P. Demediuk, R.D. Saunders, L.L. Dugan, E.D. Means, L. A. Horrocks, Spinal cord injury and protection, Ann. Emerg. Med. 14 (1985) 816–821.

[36] X. Liu, J. Sun, J. Du, J. An, Y. Li, Y. Hu, Y. Xiong, Y. Yu, H. Tian, X. Mei, C. Wu, Encapsulation of selenium nanoparticles and metformin in macrophage-derived cell membranes for the treatment of spinal cord injury, ACS Biomater. Sci. Eng. 9 (2023) 5709–5723.

[37] Y.X. Chen, T. Zuliyaer, B. Liu, S. Guo, D.G. Yang, F. Gao, Y. Yu, M.L. Yang, L.J. Du, J.J. Li, Sodium selenite promotes neurological function recovery after spinal cord injury by inhibiting ferroptosis, Neural Regen. Res. 17 (2022) 2702–2709.

[38] P. Stacey, A. Mensinkai, P. Bansal, S.H. Hosseini, A. Lavigne, B. Gwardjan, S. Leylachian, Z.J. Deng, V. Chari, S. Giles, S. Nesathurai, Using nutraceuticals to help manage traumatic spinal cord injury, Pharm. Biol. 17 (2024) 71.

[39] A. Khurana, S. Tekula, M.A. Saifi, P. Venkatesh, C. Godugu, Therapeutic applications of selenium nanoparticles, Biomed. Pharmacother. 111 (2019) 802–812.

[40] B. Xie, D. Zeng, M. Yang, Z. Tang, L. He, T. Chen, Translational selenium nanoparticles to attenuate allergic dermatitis through nrf2-keap1-driven activation of selenoproteins, ACS Nano 17 (2023) 14053–14068.

[41] Z. Zuo, M. Luo, Z. Liu, T. Liu, X. Wang, X. Huang, S. Li, H. Wu, Q. Pan, T. Chen, L. Yang, H.F. Liu, Selenium nanoparticles alleviate renal ischemia/reperfusion injury by inhibiting ferritinophagy via the XBP1/NCOA4 pathway, Cell Commun. Signal. 22 (2024) 376.

[42] S. Rao, Y. Lin, R. Lin, J. Liu, H. Wang, W. Hu, B. Chen, T. Chen, Traditional Chinese medicine active ingredients-based selenium nanoparticles regulate antioxidant selenoproteins for spinal cord injury treatment, J. Nanobiotechnol. 20 (2022) 278.

[43] J. Zhan, X. Li, D. Luo, Y. Hou, Y. Hou, S. Chen, Z. Xiao, J. Luan, D. Lin, Polydatin promotes the neuronal differentiation of bone marrow mesenchymal stem cells in vitro and in vivo: involvement of Nrf2 signalling pathway, J. Cell Mol. Med. 24 (2020) 5317–5329.

[44] A.J. Liu, J. Yu, H.Y. Ji, H.C. Zhang, Y. Zhang, H.P. Liu, Extraction of a novel cold-water-soluble polysaccharide from Astragalus membranaceus and its antitumor and immunological activities, Molecules 23 (2017) 62.

[45] C. Luo, Q. Yang, X. Lin, C. Qi, G. Li, Preparation and drug release property of tanshinone IIA loaded chitosan-montmorillonite microspheres, Int. J. Biol. Macromol. 125 (2019) 721–729.

[46] S. Min, W. Tao, Y. Miao, Y. Li, T. Wu, X. He, Y. Zhang, B. Liu, Z. Meng, K. Han, S. Liu, L. Li, J. Chen, S. Zhao, J. Zhang, X. Zhang, Dual delivery of tetramethylpyrazine and miR-194-5p using soft mesoporous organosilica nanoparticles for acute lung injury therapy, Int. J. Nanomed. 18 (2023) 6469–6486.

[47] W.J. Zhang, J.Y. Wang, H. Li, X. He, R.Q. Zhang, C.F. Zhang, F. Li, Z.L. Yang, C. Z. Wang, C.S. Yuan, Novel application of natural anisole compounds as enhancers for transdermal delivery of ligustrazine, Am. J. Chin. Med. 43 (2015) 1231–1246.

[48] H. Zhou, Q. Qian, Q. Chen, T. Chen, C. Wu, L. Chen, Z. Zhang, O. Wu, Y. Jin, X. Wang, Z. Guo, J. Sun, J. Zhang, S. Shen, X. Wang, M. Jones, M.A. Khan, P. Makvandi, Y. Zhou, A. Wu, Enhanced mitochondrial targeting and inhibition of pyroptosis with multifunctional metallopolyphenol nanoparticles in intervertebral disc degeneration, Small 20 (2024) e2308167.

[49] W. Ta, X. Li, J. Song, R. Hua, Y. Zheng, W. Lu, Customizable dual-fluorescent nanoparticles for tracing and quantifying of cell transport, Int. J. Nanomed. 18 (2023) 1823–1834.

[50] Q. Xue, H. Lai, H. Zhang, G. Li, F. Pi, Q. Wu, S. Liu, F. Yang, T. Chen, Selenium attenuates radiation colitis by regulating cGAS-STING signaling, Adv. Sci. 11 (2024) e2403918.

[51] J.J. Rennick, A.P.R. Johnston, R.G. Parton, Key principles and methods for studying the endocytosis of biological and nanoparticle therapeutics, Nat. Nanotechnol. 16 (2021) 266–276.

[52] W. Jiang, G. Huang, S. Pan, X. Chen, T. Liu, Z. Yang, T. Chen, X. Zhu, TRAIL-driven targeting and reversing cervical cancer radioresistance by seleno-nanotherapeutics through regulating cell metabolism, Drug Resist. Updates 72 (2024) 101033.

[53] D. Oprea, C.G. Sanz, M.M. Barsan, T.A. Enache, PC-12 cell line as a neuronal cell model for biosensing applications, Biosens. Bioelectron. 12 (2022) 500.

[54] Y. Ye, L. Xu, L. Zhang, P. Zhao, W. Cai, G. Fu, T. Wang, Z. Tao, W. Shi, W. Gu, J. Hu, G. Yuan, Y. Wei, K. Xu, Z. Bao, H. Chao, N. Liu, L. Zhao, Y. Tu, J. Ji, Meningioma achieves malignancy and erastin-induced ferroptosis resistance through FOXM1-AURKA-NRF2 axis, Redox Biol. 72 (2024) 103137.

[55] F. Li, H. Wang, H. Chen, J. Guo, G. Dang, Y. Ru, H. Wang, Mechanism of ferroptosis and its role in spinal cord injury, Front. Neurol. 13 (2022) 926780.

[56] Y. Ying, Z. Huang, Y. Tu, Q. Wu, Z. Li, Y. Zhang, H. Yu, A. Zeng, H. Huang, J. Ye, W. Ying, M. Chen, Z. Feng, Z. Xiang, Q. Ye, S. Zhu, Z. Wang, A shear-thinning, ROS-scavenging hydrogel combined with dental pulp stem cells promotes spinal cord repair by inhibiting ferroptosis, Bioact. Mater. 22 (2023) 274–290.

[57] W. Shen, C. Li, Q. Liu, J. Cai, Z. Wang, Y. Pang, G. Ning, X. Yao, X. Kong, S. Feng, Celastrol inhibits oligodendrocyte and neuron ferroptosis to promote spinal cord injury recovery, Phytomedicine 128 (2024) 155380.

[58] F. Ursini, M. Maiorino, Lipid peroxidation and ferroptosis: the role of GSH and GPx4, Free Radic. Biol. Med. 152 (2020) 175–185.

[59] Y. Rong, J. Fan, C. Ji, Z. Wang, X. Ge, J. Wang, W. Ye, G. Yin, W. Cai, W. Liu, USP11 regulates autophagy-dependent ferroptosis after spinal cord ischemia-reperfusion injury by deubiquitinating Beclin 1, Cell Death Differ. 29 (2022) 1164–1175.

[60] Y. Chen, X. Li, K. Luo, T. Wang, T. Liu, E. Lu, R. Wang, Y. Luo, X. Sha, Hyperthermia/glutathione-triggered ferritin nanoparticles amplify the ferroptosis for synergistic tumor therapy, Mater. Today Bio 26 (2024) 101085.

[61] Y.T. Jiao, Y.R. Kang, M.Y. Wen, H.Q. Wu, X.W. Zhang, W.H. Huang, Fast antioxidation kinetics of glutathione intracellularly monitored by a dual-wire nanosensor, Angew Chem. Int. Ed. Engl. 62 (2023) e202313612.

[62] S. Wei, T. Qiu, X. Yao, N. Wang, L. Jiang, X. Jia, Y. Tao, Z. Wang, P. Pei, J. Zhang, Y. Zhu, G. Wang, X. Liu, S. Liu, X. Sun, Arsenic induces pancreatic dysfunction and ferroptosis via mitochondrial ROS-autophagy-lysosomal pathway, J. Hazard Mater. 384 (2020) 121390.

[63] B. Wang, Y. Wang, J. Zhang, C. Hu, J. Jiang, Y. Li, Z. Peng, ROS-induced lipid peroxidation modulates cell death outcome: mechanisms behind apoptosis, autophagy, and ferroptosis, Arch. Toxicol. 97 (2023) 1439–1451.

[64] R. Yang, W. Gao, Z. Wang, H. Jian, L. Peng, X. Yu, P. Xue, W. Peng, K. Li, P. Zeng, Polyphyllin I induced ferroptosis to suppress the progression of hepatocellular carcinoma through activation of the mitochondrial dysfunction via Nrf2/HO-1/GPX4 axis, Phytomedicine 122 (2024) 155135.

[65] Y. Gong, S. Luo, P. Fan, H. Zhu, Y. Li, W. Huang, Growth hormone activates PI3K/ Akt signaling and inhibits ROS accumulation and apoptosis in granulosa cells of patients with polycystic ovary syndrome, Reprod. Biol. Endocrinol. 18 (2020) 121.

[66] A. Henn, S. Lund, M. Hedtjärn, A. Schrattenholz, P. Pörzgen, M. Leist, The suitability of BV2 cells as alternative model system for primary microglia cultures or for animal experiments examining brain inflammation, ALTEX-Altern. Anim. Ex. 26 (2009) 83–94.

[67] F.H. Brennan, Y. Li, C. Wang, A. Ma, Q. Guo, Y. Li, N. Pukos, W.A. Campbell, K. G. Witcher, Z. Guan, K.A. Kigerl, J.C.E. Hall, J.P. Godbout, A.J. Fischer, D. M. McTigue, Z. He, Q. Ma, P.G. Popovich, Microglia coordinate cellular interactions during spinal cord repair in mice, Nat. Commun. 13 (2022) 4096.

[68] H. Fan, H.B. Tang, Z. Chen, H.Q. Wang, L. Zhang, Y. Jiang, T. Li, C.F. Yang, X. Y. Wang, X. Li, S.X. Wu, G.L. Zhang, Inhibiting HMGB1-RAGE axis prevents pro-inflammatory macrophages/microglia polarization and affords neuroprotection after spinal cord injury, J. Neuroinflammation 17 (2020) 295.

[69] F.L. Wei, T.F. Wang, C.L. Wang, Z.P. Zhang, J.W. Zhao, W. Heng, Z. Tang, M.R. Du, X.D. Yan, X.X. Li, Z. Guo, J.X. Qian, C.P. Zhou, Cytoplasmic escape of

mitochondrial DNA mediated by Mfn2 downregulation promotes microglial activation via cGas-sting Axis in spinal cord injury, Adv. Sci. 11 (2024) e2305442.

[70] J. Nogueira-Rodrigues, S.C. Leite, R. Pinto-Costa, S.C. Sousa, L.L. Luz, M.A. Sintra, R. Oliveira, A.C. Monteiro, G.G. Pinheiro, M. Vitorino, J.A. Silva, S. Simão, V. E. Fernandes, J. Provazník, V. Benes, C.D. Cruz, B.V. Safronov, A. Magalhães, C. A. Reis, J. Vieira, C.P. Vieira, G. Tiscórnia, I.M. Araújo, M.M. Sousa, Rewired glycosylation activity promotes scarless regeneration and functional recovery in spiny mice after complete spinal cord transection, Dev. Cell 57 (2022) 440, 50.e7.

[71] J.Z. Li, B.Y. Fan, T. Sun, X.X. Wang, J.J. Li, J.P. Zhang, G.J. Gu, W.Y. Shen, D. R. Liu, Z.J. Wei, S.Q. Feng, Bioinformatics analysis of ferroptosis in spinal cord injury, Neural Regen. Res. 18 (2023) 626–633.